Precambrian Research 397 (2023) 107206

Contents lists available at ScienceDirect

Precambrian Research

journal homepage: www.elsevier.com/locate/precamres

Pb-Zn mineralization formed from coupled hydrocarbon-bearing and hydrothermal fluids in the Ediacaran strata in the central Sichuan Basin, China

Lianqiang Zhu [a,b], Zezhang Song [a,b,*], Guangdi Liu [a,b,*], Wenzhi Zhao [a,b], Long Wen [c], Xingwang Tian [c], Wenzhi Wang [c], Dailin Yang [c], Wei Yan [c], Qiang Li [a,b]

[a] National Key Laboratory of Petroleum Resources and Engineering, China University of Petroleum, Beijing 102249, PR China
[b] College of Geosciences, China University of Petroleum, Beijing 102249, PR China
[c] Southwest Oil and Gas Field Company PetroChina, Chengdu 610041, PR China

ARTICLE INFO

Keywords:
Metallogenesis
Hydrothermal fluid
Hydrocarbon-bearing fluid
Central Sichuan Basin

ABSTRACT

Hydrocarbon-bearing fluid plays a crucial role in the Pb-Zn mineralization process. The hydrocarbon role is still the subject of metallogenic research. This study determined the metal and sulfur sources and the hydrocarbon role in the mineralization instigated by mixing of hydrothermal and hydrocarbon-bearing fluids in the central Sichuan Basin based on petrography, fluid inclusion geochemistry, S and Pb isotope compositions, and changes in hydrocarbon phases and components. The results indicated that hydrothermal input significantly improved the salinity and temperature of reservoir fluids. Hydrothermal stages can be divided into three: (I) pyrite and dolomite, (II) quartz and sphalerite, and (III) galena. Solid bitumen was formed at stage II, and the oil inclusions were converted into gas inclusions from stage I to II, suggesting that the hydrothermal fluids caused the oil cracking. The Pb isotope compositions of pyrite, sphalerite, and galena showed that the Pb-Zn deposit had two metal sources from surface karst and hydrothermal fluids. Raman spectroscopy and sulfur isotope compositions implied that H_2S formed during hydrothermal input was generated from TSR resulting from hydrothermal sulfate. The H_2S produced by TSR preferentially led to the precipitation of metals (Pb, Zn, and Fe) derived from the hydrothermal fluid, followed by the precipitation of metals derived from the karst fluid. After the metal elements in the reservoir were depleted, the remaining H_2S was conserved together with the natural gas in the reservoir. This study unravels the transformation of oil to gas and the H_2S generation in the reservoir through hydrocarbon inclusion analysis in the metallogenic study, providing new insight into the Pb-Zn mineralization involving hydrocarbon-bearing fluid participation.

1. Introduction

The Mississippi Valley-type (MVT) deposits found on all continents are among the most essential Pb-Zn deposits in the world (Leach et al., 2005; Leach and Bradley, 2010; Sośnicka and Lüders, 2019). The geological and geochemical characteristics of MVT deposits, the source and mobilization of metal elements, the migration and precipitation mechanism, the mineralization age, and the mineralization dynamics are the significant achievements in MVT deposit-related research to date (Leach et al., 2005; Anderson, 2008, 2015a; Hurtig et al., 2018; Li et al., 2021). The hydrocarbon fluids (oil and gas) could play a crucial role in the Pb-Zn mineralization process, which is one of the essential conclusions (Ostendorf et al., 2015; Lecumberri-Sanchez et al., 2018; Fazlia et al., 2019).

Hydrocarbon-bearing fluid is an organic matter-rich geological fluid, generated from the thermal evolution of sedimentary organic matters at specific temperatures and pressures. It is an important endogenous geological fluid in sedimentary basins (Burruss, 1981; Bodnar, 1990). Numerous studies have demonstrated close relationships between hydrocarbon inclusions in minerals, solid bitumen seams, oil field location, and Zn-Pb mineralization (MacQuee and Powell, 1983; Eisenlohr et al., 1994; Giordano, 2002; Selby et al., 2005; Wu et al., 2013; Pelch et al., 2015). Hydrocarbons have been speculated as possible reducing agents in MVT deposit mineralization processes (Kesler et al., 1994; Sicree and

* Corresponding authors.
E-mail addresses: songzz@cup.edu.cn (Z. Song), lgd@cup.edu.cn (G. Liu).

https://doi.org/10.1016/j.precamres.2023.107206
Received 19 March 2023; Received in revised form 4 October 2023; Accepted 6 October 2023
Available online 12 October 2023

Barnes, 1996; Chi et al., 2004; Wu et al., 2013; Anderson, 2015; Saintilanet al., 2016). The thermochemical sulfate reduction (TSR) of organic matters (oil and gas) could supply sufficient reducing sulfur for mineralization at a high temperature (>150 °C) (Ohmoto, 1972, 1986; Ohmoto et al., 1979; Kiyosu, 1980; Leach et al., 2005). The thermal cracking of sulfur-containing organic matters could also produce H_2S, resulting in metal precipitation (Wu et al., 2013). Hydrocarbon-bearing fluids play essential roles in these two H_2S production processes. However, the convergence dynamic of ore-forming fluids and endogenous fluids in the basin under the foreland evolution background is poorly understood. Further research is required to determine the hydrocarbon-bearing fluid role in mineralization and the relationship between the formation and destruction of oil and gas reservoirs and Pb-Zn mineralization. It is still mandatory to determine the direct involvement of hydrocarbons in metal precipitation and clarify the fundamental interaction between ore-forming fluids and hydrocarbons.

The Sichuan-Yunnan-Guizhou Pb-Zn polymetallic metallogenic belt is an important Pb-Zn mineralization area in China. The MVT deposits in this region are hosted by carbonate rocks (Wang et al., 2013; Luo et al., 2022; Yuan et al., 2014a,b; Zhao et al., 2021). In many Pb-Zn deposits, including Chipu and Daliangzi, black carbonaceous fracture zones and blackening phenomena resulting from organic matters appeared in the surrounding rocks near the ore bodies, and a large amount of solid bitumen was found in the deposits, indicating that the Pb-Zn mineralization was linked with hydrocarbon-bearing fluids (Chen, 1986; Li, 2002; Zhang et al., 2008). The Ediacaran Dengying (DY) and lower Cambrian Longwangmiao (LWM) formations in the central Sichuan Basin are the principal producing layers of the Anyue gas field, buried more than 4500 m. In contrast to the surface-near-surface deposits, except for Pb-Zn ore and solid bitumen, the DY and LWM formations are rich in natural gas. Carbon and sulfur isotope compositions of solid bitumen and gas composition proved the presence of TSR in the DY reservoir (Zhu et al., 2015; Zhang et al., 2019). Moreover, Pb-Zn ore coexists with solid bitumen and natural gas in the reservoir (Jiang et al., 2016; Feng et al., 2017; Zhang et al., 2019); consequently, a few scholars speculate that Pb-Zn mineralization may be linked with TSR (Zhang, 2019). However, the hydrocarbon contribution in the MVT deposits is not discussed systematically, and more evidence is required to examine the hydrocarbon role and mineralization process. Natural gas, solid bitumen, and Pb-Zn ore retain much geochemical data about Pb-Zn mineralization. Therefore, this Pb-Zn deposit is an ideal object for studying "oil and gas accumulation and metal mineralization" (Cheng et al., 2009).

Based on petrography of the Pb-Zn deposits, fluid inclusion geochemistry, and S-Pb isotope compositions, the metal and sulfur sources and the hydrocarbon role in the mineralization processes were determined. This study discussed the potential hydrocarbon role in the Pb-Zn mineralization in the Sichuan-Yunnan-Guizhou Pb-Zn polymetallic metallogenic belt.

2. Geological setting

The Anyue Ediacaran-Lower Cambrian gas field is located in the central Sichuan Basin in southern China. The DY and the LWM formations comprising marine carbonate rocks are the primary gas-producing layers (Du et al., 2014; Xu et al., 2014; Zhu et al., 2015). The DY

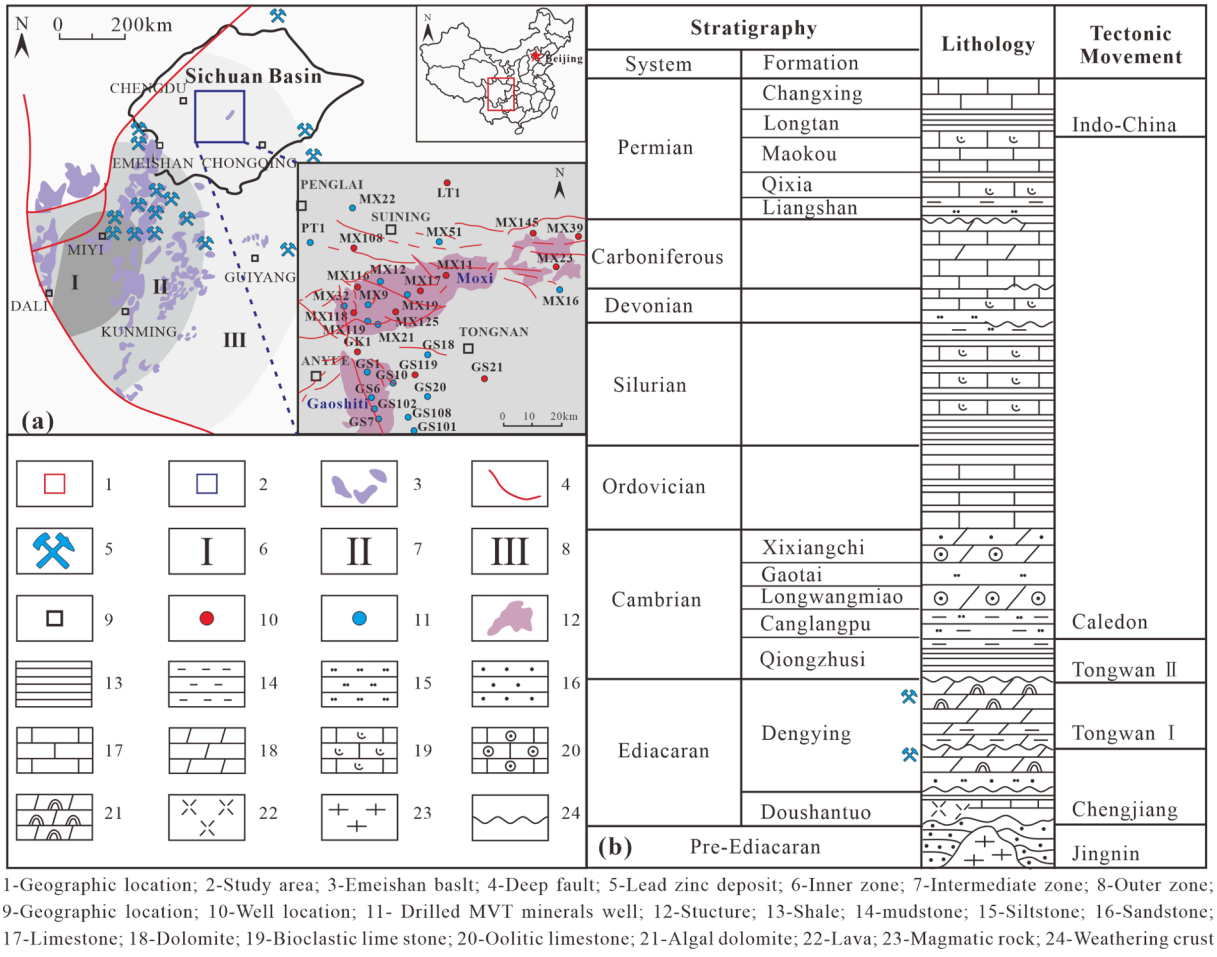

1-Geographic location; 2-Study area; 3-Emeishan baslt; 4-Deep fault; 5-Lead zinc deposit; 6-Inner zone; 7-Intermediate zone; 8-Outer zone; 9-Geographic location; 10-Well location; 11- Drilled MVT minerals well; 12-Stucture; 13-Shale; 14-mudstone; 15-Siltstone; 16-Sandstone; 17-Limestone; 18-Dolomite; 19-Bioclastic lime stone; 20-Oolitic limestone; 21-Algal dolomite; 22-Lava; 23-Magmatic rock; 24-Weathering crust

Fig. 1. Geological setting of the central Sichuan Basin. (a) The location of the study area and wells drilling into MVT deposits (Modified based on He et al., 2003; Feng et al., 2017); (b) Stratigraphic column for the central Sichuan Basin (Modified based on Yang et al., 2018).

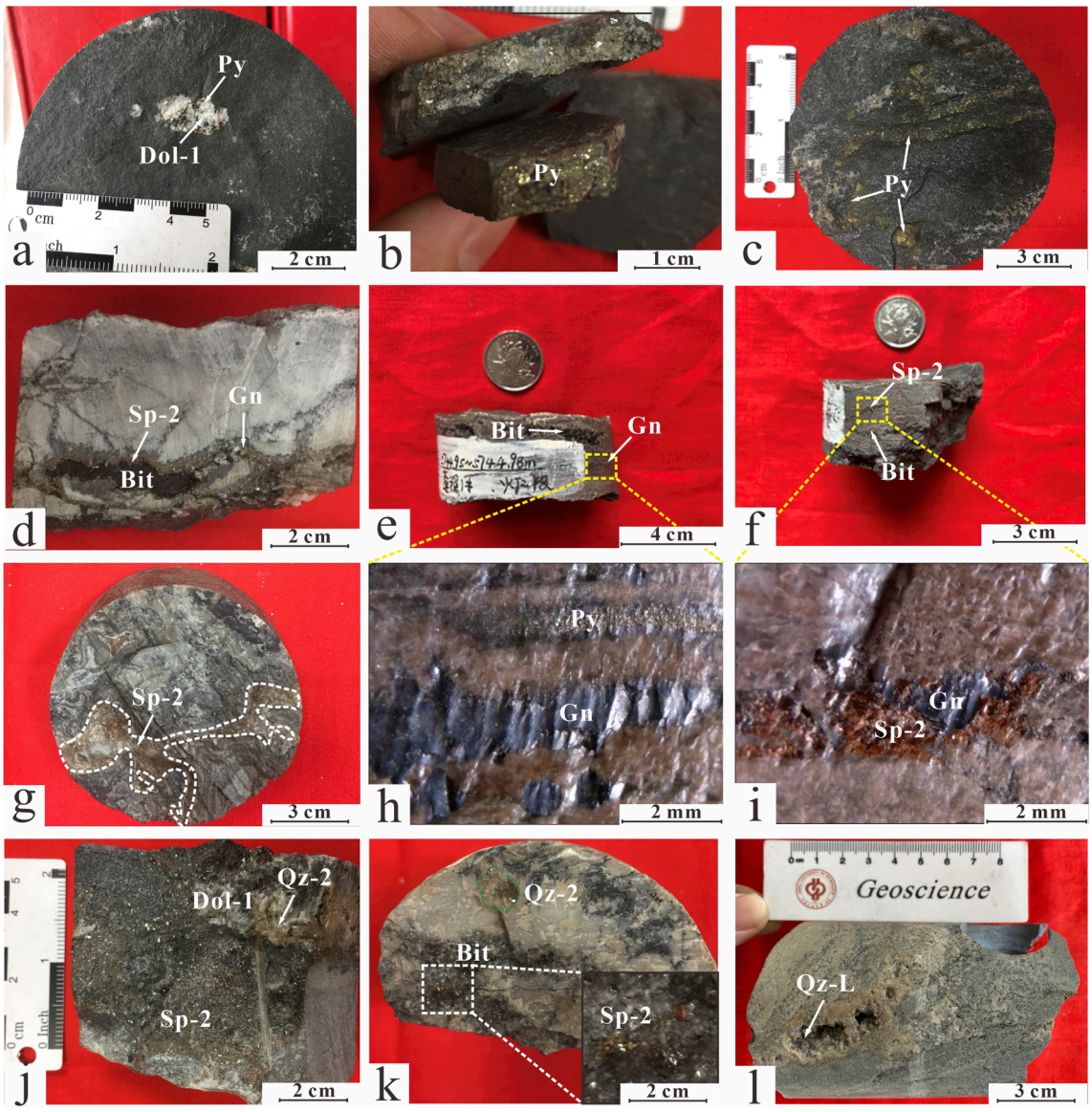

Fig. 2. Drill cores of altered rocks in the DY and LWM formations *(a) LT1, 5475.63 m, LWM, Dol-1 dolomite and pyrite filling the pore; (b) LT1, 5476.48 m, LWM, massive pyrite filling the crack; (c) GS7, 5264.67 m, D-4, dolomite replaced by massive pyrite; (d) GS101, 5250 m, D-4, massive solid bitumen and Pb-Zn veins filling the fractures; (e) GS7, 5293.44 m, D-4, pyrite, galena, and solid bitumen filling the pores; (f) GS6, 5365 m, D-2, sphalerite and galena filling the pores; (g) PT1, 5775.12 m, D-2, sphalerite filling the algal-framed pores; (h) GS7, 5293.44 m, D-4, partial enlargement of e, pyrite, galena and solid bitumen filling the pores; (i) GS6, 5365 m, D-2, partial magnification of f, sphalerite and galena filling the pores; (j) GS7, 5293.16 m, D-4, Pb-Zn veins and gangue minerals such as dolomite and quartz; (k) GS124, 5605.57 m, D- 2, The Qt-2 quartz, solid bitumen, and galena filling the pores; (l) GS6, 5034.78 m, coarse-grained euhedral quartz developed on the edge of the pores. Abbreviations: Dol-dolomite, Py- pyrite, Sp-sphalerite, Gn-galena, Qz-quartz; Bit-solid bitumen.*

Formation is further divided into four members from the bottom to the top, D-1, D-2, D-3, and D-4 (Zhou et al., 2017; Yang et al., 2018, 2023). Many pores developed in the D-2 and D-4 members during the Tongwan tectonic movement, providing adequate porosity for the subsequent oil and gas charging (Zou et al., 2014; Luo et al., 2015) (Fig. 1). Previous studies have demonstrated that large-scale paleo-oil reservoirs formed in the DY Formation of the central Sichuan Basin. The natural gas and solid bitumen in the reservoirs were cracked from the crude oil in the paleo-oil reservoirs (Gao et al., 2017; Zhang et al., 2019; Zhu et al., 2015, 2022; Yang et al., 2023).

The Emeishan mantle plume resides southwest of the Sichuan Basin. The Emeishan Great Igneous Rock Province is roughly divided into three zones from west to east: the inner (deep denudation zone), the middle (partial denudation zone), and the outer (ancient weathering crust zone) (He et al., 2003) (Fig. 1a). The study area is located in the outer zone. The mantle plume caused hydrothermal activity in the Sichuan Basin, resulting in extensive hydrothermal mineralization (Boven et al., 2002; Zhang et al., 2013; Yuan et al., 2014; Chen et al., 2012; Feng et al., 2017) (Fig. 1a). The DY Formation in the central Sichuan Basin is 500 to 800 m thick (Zhang, 2019), providing necessary host rocks for large-scale Pb-Zn mineralization. Numerous fractures and pores in the strata serve as channels for ore-forming fluid migration. Simultaneously, the overlying Qiongzhusi shales are efficient barriers to prevent the ore-forming fluids from evading upward (Fig. 1b). Pb-Zn mineralization predominantly occurred in the DY Formation, with sporadic occurrences in the LMW Formation. The Pb-Zn ores were found in more than ten wells (such as GS7 and GS6) in the central Sichuan Basin at a depth of over 4500 m (Feng et al., 2017; Zhang, 2019) (Fig. 1a). Pb-Zn ore occurs predominantly in the algal dolomite strata of the D-2 and D-4, replacing the dolomite or filling the pores (Feng et al., 2017; Zhang, 2019). The mineral assemblage is simple, comprising pyrite, galena, sphalerite, dolomite, quartz, and anhydrite, typically associated with solid bitumen

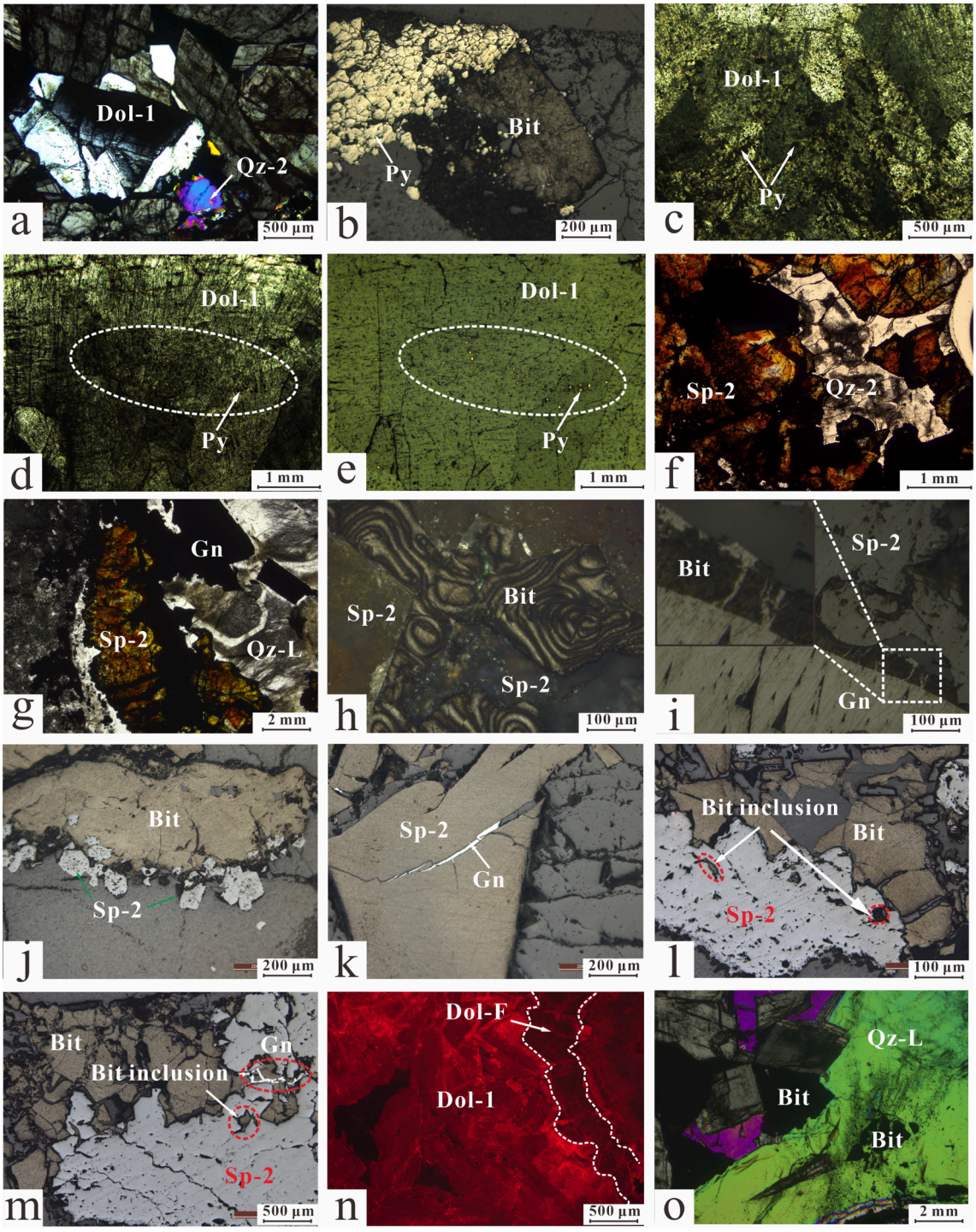

Fig. 3. Features of different minerals under a microscope *(a) PT1, 5789.72 m, D-2, Dol-1 with curved crystal planes and wavy extinction, Qz-2 filling the intercrystalline pores of Dol-1; (b) PT1, 5745.89 m, D-2, pyrite and solid bitumen filling pores, with host rock replaced by granular pyrite; (c-e) GS 10, 5196.7 m, D-4, c and d transmitted light, e reflected light, granular pyrite replacing Dol-1; (f) GS7, 5293.2 m, D-4, solid bitumen, co-existing Qz-2 and Sp-2; (g) GS7, 5293.16 m, D-4, sphalerite, galena and quartz filling pores and galena replacing host rock; (h) GS7, 5293.16 m, D-4, co-existing fibrous solid bitumen and Sp-2; (i) GS7, 5293.16 m, D-4, solid bitumen, Sp-2, and galena filling pores, and galena filling cracks within the solid bitumen; (j) MX145, 5659.87 m, D-4, granular sphalerite replacing the host rock, and solid bitumen filling pores; (k) MX145, 5587.28 m, D-4, the mosaic solid bitumen filling pores and galena filling in the cracks within the solid bitumen; (l) MX145, 5662.73 m, D-4, mosaic solid bitumen and Sp-2 filling pores and bitumen inclusions in the Sp-2; (m) MX145, 5659.87 m, D-4, co-existing mosaic solid bitumen, sphalerite, galena filling cracks within the solid bitumen, and solid bitumen inclusions in the Sp-2; (n) PT1, 5780.74 m, D-2, Dol-F with dull luminescence developed at the edge of pores and Dol-1 with dark red luminescence; (o) PT1, 5778.57 m, D-2, Qz-L filling the entire pore space and solid bitumen inclusions in the quartz. Abbreviations: Dol-dolomite, Py- pyrite, Sp-sphalerite, Gn-galena, Qz-quartz; Bit-solid bitumen.* (For interpretation of the references to colour in this figure legend, the reader is referred to the web version of this article.)

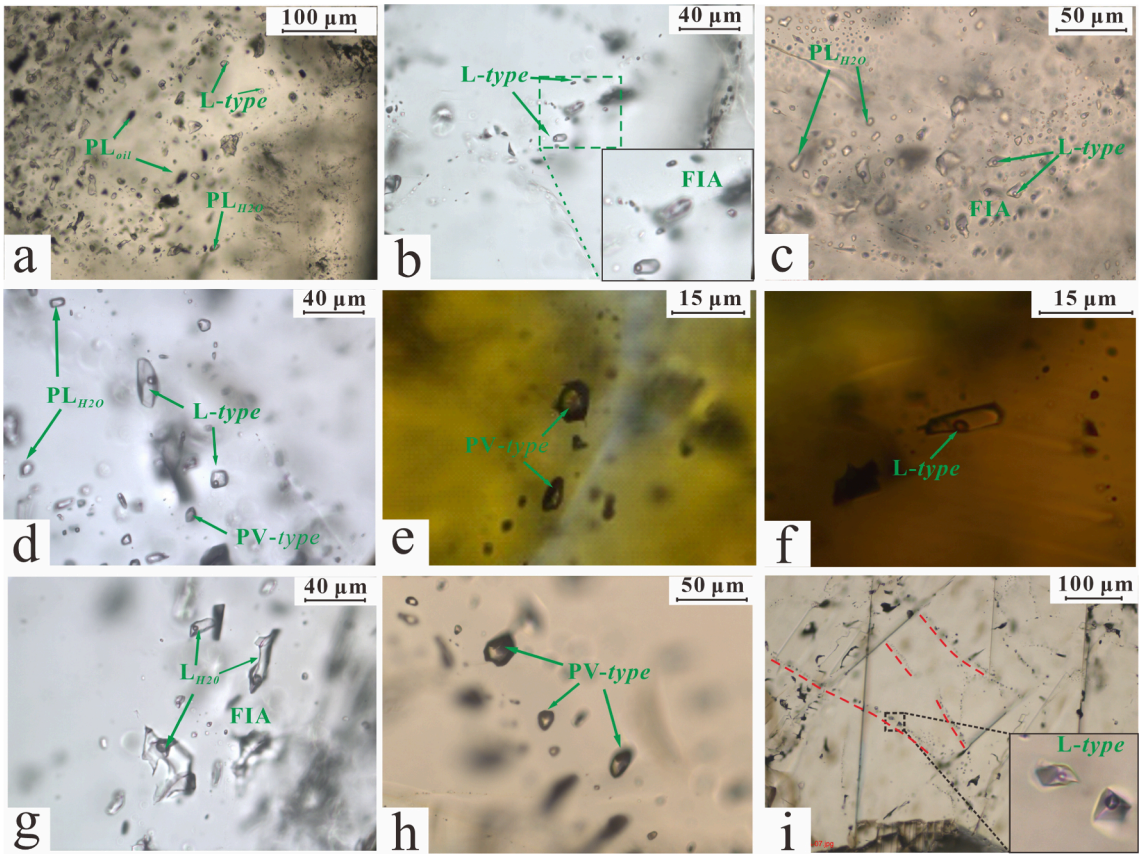

Fig. 4. Micrograph of fluid inclusions in dolomite, quartz, and *sphalerite (a) GS7, 5263.88 m, D-4, Brown oil inclusions (PL$_{oil}$), light grey pure water inclusions (PL$_{H2O}$), and liquid-rich two-phase inclusions (L-type) in Dol-F dolomite; (b) PT1, 5789.72 m, D-2, liquid-rich two-phase fluid inclusion assemblages (L- type FIA) in Dol-1 dolomite; (c) PT1, 5780.74 m, D-2, Light grey PL$_{H2O}$ inclusions and L-type FIA in Qz-2 quartz; (d) PT1, 5780.74 m, D-2, Light grey PL$_{H2O}$ inclusions and L-type inclusions in Qz-2 quartz; (e-f) GS7, 5311.57 m, D-4, dark grey pure gas inclusions (PV-type) and L-type inclusions in Sp-2 sphalerite; (g) PT1, 5778.57 m, D-2, L-type FIA in Qz-L quartz; (h) MX145, 5662.73 m, D-4, dark grey PV-type inclusions in Qz-L quartz; (i) GS7, 5259.8 m, D-4, secondary L-type inclusions distributed in bands which penetrate crystal boundary;*

and natural gas (Jiang et al., 2016; Feng et al., 2017; Zhang, 2019). The hydrothermal alteration of surrounding rocks includes silicification and dolomitization (Jiang et al., 2016; Zhang, 2019).

3. Samples and methods

3.1. Sampling and sample preparation

Drill core sampling. The burial depth of the DY Formation in the central Sichuan Basin exceeds 4500 m, and Pb-Zn ore sampling is exclusively performed on drill cores, which makes sampling more challenging. More than 20 Pb-Zn ore-enriched dolomite samples were collected through the observing drill cores from 30 drill holes in the central Sichuan Basin. The samples were primarily from 8 drill holes, including five wells in the Gaoshiti area (GS6, GS7, GS20, GS108, GS101) and three in the Moxi area (MX9, MX12, MX32). All samples were collected from the D-2 and D-4 members.

Sample preparation. Dolomite samples containing pyrite, sphalerite, and galena were cut into 20 × 20 mm sheet samples and then administered to coarse and fine polishing on a grinding and polishing machine using alumina mortar. The samples were polished with 1.0 and 0.3 μm alumina suspensions using a flannel polishing fabric. The samples were subsequently adhered to glass slides using epoxy. After drying, samples were ground to approximately 0.3 mm for petrographic analysis. Nine dolomite samples containing high concentrations of pyrite, galena, and sphalerite were crushed to particles of 10–30 mesh. Then, pure pyrite, galena, and sphalerite particles were selected under a microscope and ground to 200 mesh for geochemical analysis.

3.2. Experimental method

Petrographic analysis. Macroscopic petrographic analysis was performed on drill cores from 30 wells. Microscopic petrographic analysis was performed on thin sections using a Leica DM 4500P microscope equipped with transmitted and reflected lights at the State Key Laboratory of Petroleum Resources and Exploration at the China University of Petroleum (Beijing),. Cathodoluminescence analysis was performed utilizing a CL8200 MK5 cathodoluminescence microscope with a 9–11 kV beam voltage and a 300 μA beam current.

Fluid inclusions. Fluid inclusions were analyzed at the Beijing Institute of Geology of Nuclear Industry, China. Sphalerite, dolomite, and quartz were selected for fluid inclusion analysis. Homogenization temperature and salinity were measured using a LINKAM THMSG600 heating-freezing stage. Micro-thermometric measurements were performed on primary liquid-rich fluid inclusions in dolomite, quartz, and sphalerite, and all fluid inclusions were homogenized to the liquid phase during heating and the solid phase during cooling. The measuring temperature ranged from –195 ℃ to 600 ℃, with a heating rate of 10 ℃/min and a cooling rate of 0.2 ℃/min. The room temperature was 25 ℃, and the humidity was 50 %. A Horiba LabRAM 800 research-grade micro-laser Raman spectrometer equipped with a YAG crystal frequency-doubled solid-state laser with a 532 nm wavelength was used for fluid inclusion composition investigation. The fluid density was calculated with Flincor software using homogenization temperature and salinity of fluid inclusion following the H_2O-NaCl system.

Pb isotope analysis. One galena sample, two pyrite samples, and two sphalerite samples were selected for Pb isotope analysis ($^{208}Pb/^{204}Pb$,

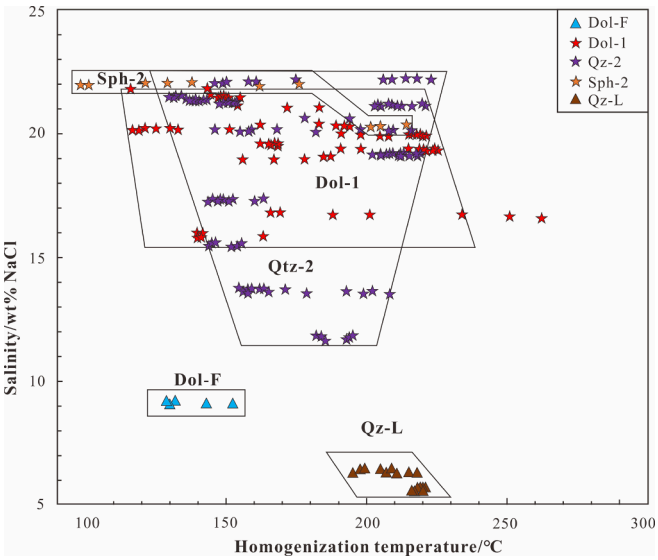

Fig. 5. Homogenization temperatures and salinities of fluid inclusions in quartz, sphalerite, and dolomite.

$^{207}Pb/^{204}Pb$, $^{206}Pb/^{204}Pb$). Pb isotope analysis was performed at the Beijing Institute of Geology of Nuclear Industry, China. The powder sample was dissolved using HF-HNO_3 mixing acid and evaporated. After evaporation, the evaporated sample was converted into chloride using 6 M HCl and then extracted with 0.6 M HBr. The Pb sample was eluted and separated using 0.6 M HBr and 6 M HCl on an exchange column containing 150 μL of AGx8 ion exchange resin. The background of the Pb treatment process was less than 200 pg. The Pb sample was then subjected to an ISOPROBE-T thermal surface ionization mass spectrometer for Pb isotope analysis. The room temperature was 20 ℃, and the humidity was 30 %. The analysis accuracies are better than 0.03 % (2σ).

Sulfur isotope analysis. Three pyrite, three sphalerite, and three galena samples were selected for sulfur isotope analysis. Sulfur isotope analysis was conducted at the Beijing Institute of Geology of Nuclear Industry, China. The sulfide mineral powder and copper oxide were mixed and heated to 1100 ℃ in a vacuum to convert the sulfur in the sulfide mineral into SO_2. The sample tube was frozen with liquid nitrogen to remove impure gases from the SO_2. The SO_2 was then passed into a Delta-v plus gas isotope mass spectrometer for sulfur isotope composition analysis. The stable sulfur isotope analysis results were standardized using V-CDT (‰).

4. Results

4.1. Filling characteristics

The Pb-Zn ore is localized at the Moxi-Gaoshiti area and distributed in layers along the top of the D-2 and D-4. The Pb-Zn mineralization is subjected to deep faults (Fig. 1a). Two types of primary ores are identified, including massive and veined ores, and comprise galena, sphalerite, and pyrite (Fig. 2). The ores primarily replace the algal dolomite or occupy the pores and cracks, exhibiting epigenetic characteristics (Fig. 2). The predominant ore textures are granular and metasomatic. The hydrothermal alteration includes dolomitization and silicification, forming a substantial quantity of dolomite and quartz (Fig. 2a, d, j).

The hydrothermal stage may be divided into three based on the observed mineralogy and symbiotic relationship between sulfide and gangue minerals in cores and thin sections. Stage I is recognized by saddle dolomite (Dol-1) and pyrite (Fig. 2a; Fig. 3a-e). Dol-1 has a curved crystal plane and exhibits wavy extinction under cross-polarized light; pyrite has a granular texture, typically formed at the edge of pores and occasionally replacing host rocks and Dol-1 (Fig. 3b-e). Furthermore, some fine-grained dolomites (Dol-F) grow along the pore edge, in contact with Dol-1, and exhibit dull cathodoluminescence differing from Dol-1 (Fig. 3n). Stage II is identified by quartz (Qz-2) and sphalerite (Sp-2) and is the primary Zn mineralization stage. Qz-2 possesses a euhedral granular texture (Fig. 3a, f) and occupies the intercrystalline pores of Dol-1 (Fig. 3a). Sp-2 has a granular texture, tending to fill pores or replace host rocks, and appears dark brown under polarized light

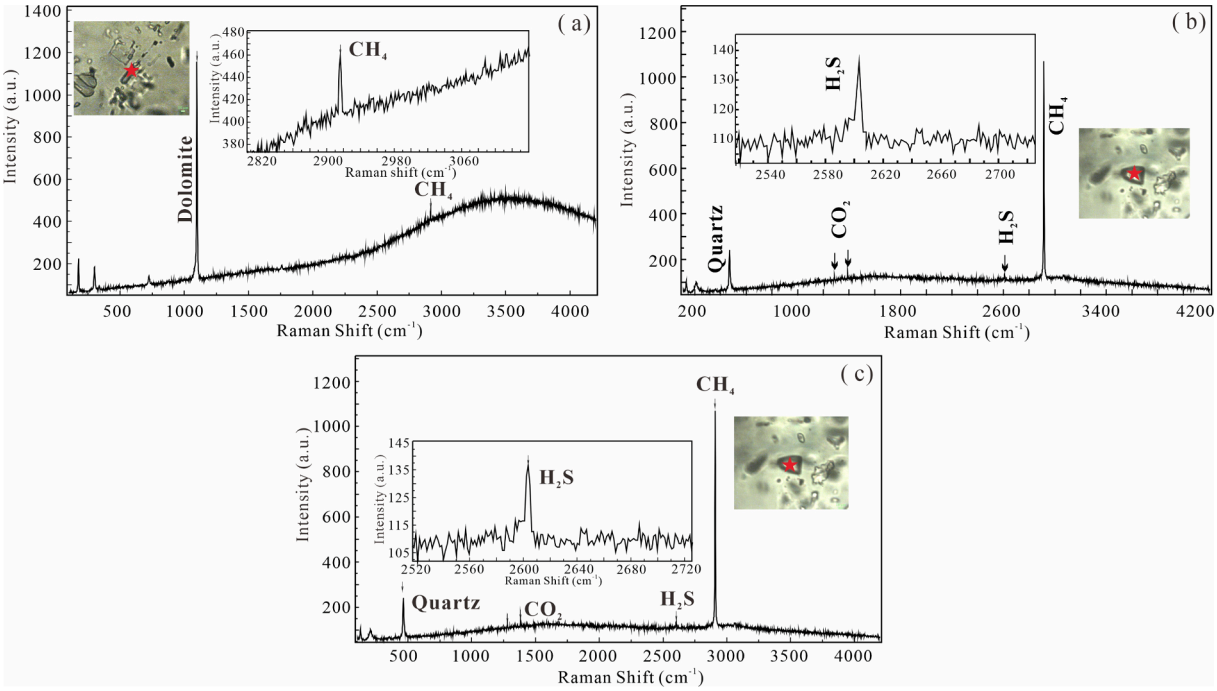

Fig. 6. Laser Raman spectra of fluid inclusions in quartz and dolomite *(a) PT1, 5780.74 m, D-2, the gas phase of the L-type inclusions in Dol-F consists of CH4; (b) GS7, 5290.5 m, D-4, gas inclusions in Qz-2 are primarily composed of CH_4, H_2S, and CO_2; (c) PT1, 5727.67 m, D-2, Gas in PV-type inclusions in the Qz-L quartz consists of CH_4, H_2S, and CO_2.*

Table 1
Sulfur isotope compositions of pyrite, sphalerite, and galena.

	Formation	Depth	Sulfide mineral	$\delta^{34}S_{V\text{-}CDT}$
GS7-1	D-4	5341.0	pyrite	28.6
GS108-1	D-4	5334.0		17.9
GS101-1	D-4	5490.0	sphalerite	27.2
MX32-1	LWM	4661.2		29.3
GS101-2	D-4	5488.0		25.5
GS6-1	D-2	5362.1	galena	26.7
MX12-1	D-4	5234.5		24.4
MX9-1	D-2	5444.6		22.5
GS7*	D-4	5293.2	pyrite	19.6
GS20*	D-4	5255.3		19.2
MX9*	D-4	5312.3		16.1
GS1*	D-4	4957.2	sphalerite	24.0
GS1*	D-4	4957.2		23.7
GS7*	D-4	5293.2		23.5
MX9*	D-2	5444.6		25.0
GS1*	D-4	4957.2	galena	19.1
GS1*	D-4	4957.2		19.0
GS7*	D-4	5293.2		20.0
GS18*	D-4	5143.7		21.5
MX9*	D-2	5444.6		20.0

Note: Data with "*" are quoted from Zhang (2019).

(Fig. 3f-m). A large amount of solid bitumen (Bit) was observed co-existing with Sp-2. Solid bitumen adheres to the surface of Sp-2 (Fig. 3h) or can exist as inclusions within the sphalerite (Fig. 3l, m), suggesting that both phases formed simultaneously. The solid bitumen has optical anisotropy and shows mosaic and fibrous textures (Fig. 3h-m). Stage III is characterized by galena. Galena exhibits a massive texture, replaces Sp-2 or occupies the cracks within solid bitumen, indicating that it formed after the solid bitumen (Fig. 3g, i, k, m). Some quartz (Qz-L) formed after galena is also present in the reservoir (Fig. 2l, Fig. 3o).

4.2. Fluid inclusions

4.2.1. Classification strategy

Geochemical analyses of fluid inclusions in dolomite, quartz, and sphalerite have been conducted (including hydrothermal and non-hydrothermal minerals). Primary inclusions occurring as isolated, random, clusters, along growth zones, and fluid inclusion assemblages (FIAs) were analyzed according to Bodnar (2003). Based on the phase ratio at room temperature and the phase transition during cooling and heating, three types of primary inclusions were identified in dolomite, sphalerite, and quartz, including liquid-rich two-phase inclusions (L-type), pure liquid phase inclusions (PL-type), and pure gas-phase inclusions (PV-type) (Fig. 4).

L-type inclusions are generally oval, elongated, diamond-shaped, or irregular ranging from 2 to 40 μm in size, typically between 5 and 10 μm (Fig. 4a-d, f, g). These inclusions contain liquid and gas phases, with gas bubbles accounting for 5 %-10 % of the inclusion volume (Fig. 4b-d). Certain secondary L-type inclusions penetrate crystal boundaries (Fig. 4i). PL-type inclusions can be further divided into pure water inclusions (PL_{H2O}) and oil inclusions (PL_{oil}). PL_{H2O} inclusions are randomly distributed and typically co-exist with L-type inclusions. They are square or irregular in shape and range from 1 to 10 μm in size (Fig. 4c). Dark-colored PL_{oil} inclusions are typically elliptical or irregular in shape and range from 1 to 8 μm in size. Gray PV-type inclusions are irregular, oval, or round in shape and range from 1 to 12 μm in size. Dol-F primarily trapped PL_{oil} and L-type inclusions. Dol-1 trapped the same fluid inclusion assemblage as Dol-F, whereas Sp-2 and Qz-2 primarily trapped PV-type and L-type inclusions. Qz-L primarily trapped PV-type and L-type inclusions as Sp-2 and Qz-2.

4.2.2. Microthermometry and Raman spectroscopy

Dol-F dolomite predominantly trapped brown pure oil inclusions (PL_{oil}) and grey L-type inclusions. The homogenization temperature of L-type inclusions ranged from 129 to 152 °C, whereas the salinity and density ranged from 9.1 to 9.2 wt% NaCl eq and 0.98 to 1.00 g/cm^3, respectively. In Stage I, Dol-1 dolomite trapped grey L-type inclusions and a few V-type inclusions. The homogenization temperature of the L-type inclusions was from 116 to 262 ℃, whereas the salinity varied from 16.6 to 21.8 wt% NaCl eq and the density from 0.93 to 1.10 g/cm^3. Qz-2 quartz trapped grey L-type inclusions and a few V-type inclusions. The homogenization temperature of L-type inclusions had a range of 130 to 223 ℃, whereas the salinity was distributed from 11.7 to 22.2 wt% NaCl eq and the density from 0.96 to 1.09 g/cm^3. In Stage II, Sp-2 sphalerite primarily trapped grey L-type inclusions and dark grey PV-type inclusions. The homogenization temperature of the L-type inclusions was between 98 and 214 ℃, whereas the salinity and density were from 20.3 to 22.0 wt% NaCl eq and 1.01 to 1.10 g/cm^3 respectively. Qz-L quartz primarily trapped grey L-type inclusions and dark grey PV-type inclusions. The homogenization temperature of the L-type inclusions fluctuated between 195 and 221 °C, whereas the salinity scattered between 5.6 and 6.5 wt% NaCl eq and the density between 0.89 and 0.90 g/cm^3 (Fig. 5). The salinities of fluid inclusions trapped in Dol-F dolomite and Qz-L quartz are uniform, and the homogenization temperatures have a limited range. Conversely, the temperatures and salinities of fluid inclusions trapped in Dol-1, Qz-2, and Sp-2 cover a broad range (Fig. 5).

Laser Raman analysis was performed on the fluid inclusions in Dol-1 and Qz-L. The results showed that the gas phase of the L-type inclusions in Dol-1 was primarily CH_4, and the concentrations of other components did not reach their detection limits. The PV-type inclusions in Qz-2 and Qz-L quartz consisted of CH_4, H_2S, and CO_2 (Fig. 6).

4.3. S and Pb isotope compositions

The sulfur isotope compositions of sulfide minerals range from 16.1 ‰ to 29.3 ‰, exhibiting strong positive bias, consistent with the reported data (Zhang, 2019) (Table 1). Pyrite, sphalerite, and galena possess sulfur isotope compositions ranging from 16.1 ‰ to 28.6 ‰ (mean value of 20.3 ‰), 23.5 ‰ to 29.3 ‰ (mean value of 25.5 ‰), and 19.0 ‰ to 26.7 ‰ (mean value of 21.7 ‰), respectively. Pyrite and galena have comparable sulfur isotope compositions, whereas sphalerite is more enriched in ^{34}S (Table 1).

The $^{208}Pb/^{204}Pb$, $^{207}Pb/^{204}Pb$, and $^{206}Pb/^{204}Pb$ of sulfide minerals vary from 37.847 to 38.492, 15.623 to 15.731, and 17.866 to 18.357, respectively, and the analysis accuracies are better than 0.03 % (2σ). The value range of Pb isotopes is limited, and the difference in each Pb isotope ratio is less than 1 %. According to the distribution characteristics of Pb isotopes, these sulfide minerals can be further divided into two categories. The $^{208}Pb/^{204}Pb$, $^{207}Pb/^{204}Pb$, and $^{206}Pb/^{204}Pb$ of the first type ranged from 37.847 to 38.038, 15.623 to 15.681, and 17.866 to 17.955, respectively, and the difference of the isotopes is less than 0.2 %; whereas these of the second type range from 38.384 to 38.492, 15.695 to 15.731, and 17.328 to 18.357, respectively, and the difference of the isotopes is less than 0.2 % (Table 2).

5. Discussion

5.1. Hydrothermal activity and solid bitumen formation

Dol-F formed earlier than Dol-1 and grew regularly along pore edges. It also has lower homogenization temperature (similar to burial temperature in Late Permian) and salinity than hydrothermal Dol-1 and sphalerite, suggesting that Dol-F formed before hydrothermal activity. Qz-L is recognized by coarse-grained, high homogenization temperature, and low salinity, widely occurring in the DY reservoir (Liang, 2014; Su et al., 2020; Fan et al., 2022). The Himalayan tectonic movement resulted in temperature and pressure variations that led to the formation of Qz-L (Jia, 2007; Liu et al., 2008; Yang et al., 2016a, b). The burial depth of 6000 m after the Cretaceous resulted in similar homogenization

Table 2
Pb isotope ratios of pyrite, sphalerite, and galena.

Sample	Depth	Formation	Sulfide mineral	$^{208}Pb/^{204}Pb$	Std err	$^{207}Pb/^{204}Pb$	Std err	$^{206}Pb/^{204}Pb$	Std err
GS7-1	5341.0	D-4	pyrite	37.936	0.005	15.659	0.001	17.919	0.001
MX32-1	4661.2	LWM		38.384	0.015	15.695	0.005	18.328	0.005
GS108-1	5334.0	D-4	sphalerite	37.847	0.002	15.623	0.001	17.89	0.001
GS101-1	5491.1	D-4		37.880	0.007	15.648	0.002	17.866	0.003
GS101-2	5488.0	D-4		37.949	0.004	15.666	0.002	17.877	0.002
GS108-2	5333.5	D-4		37.985	0.006	15.662	0.002	17.918	0.002
MX9-1	5444.6	D-2		38.011	0.006	15.674	0.002	17.925	0.003
GS1-1	4957.2	D-4		38.038	0.008	15.681	0.003	17.955	0.003
GS101-3	5490.0	D-4	galena	38.492	0.023	15.731	0.009	18.357	0.01

temperatures of fluid inclusions in Qz-L to hydrothermal fluids.

The oil inclusions trapped in Dol-F indicate that crude oil charging occurred before hydrothermal input. The homogenization temperatures of the L-type inclusions in Dol-F (129–152 ℃) correspond to Late Permian according to the burial history of strata in central Sichuan (Su et al., 2020), indicating that crude oil charging occurred in the Late Permian. Numerous works on isotope compositions and components of natural gas and solid bitumen distribution have shown that the DY solid bitumen primarily originated from crude oil cracking (Xu et al., 2014; Wei et al., 2015; Zhu et al., 2015; Zhu et al., 2022). Based on the analysis of the filling sequences between hydrothermal minerals (Dol-1, Qz-2, Sp-2, and galena) and solid bitumen, solid bitumen formed during Stage II. Furthermore, hydrocarbon inclusions analysis revealed that oil transformed into natural gas during Stage II (Fig. 4a, d, e), indicating oil cracking. Dol-1 has the same coarse-grained, curved crystal faces, and red cathodoluminescence as the saddle dolomite used for in-situ U-Pb dating to estimate the hydrothermal time (Su et al., 2020). The dating results revealed that hydrothermal activity occurred at 259.4 Ma, highly consistent with the occurring time of the Emeishan mantle plume (259.1 Ma) (Su et al., 2020). The burial history of strata showed that the DY

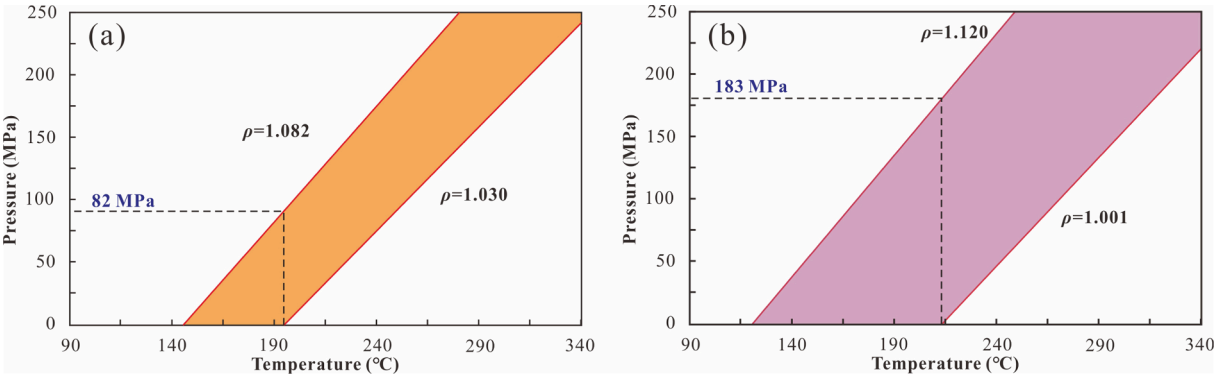

Fig. 7. Formation pressure estimation of DY Formation (Calculated with Flincor) *(a) The reservoir pressure was about 82 MPa when Dol-1 formed at Stage I; (b) The f reservoir pressure was about 183 MPa when Sp-2 formed at Stage II.*

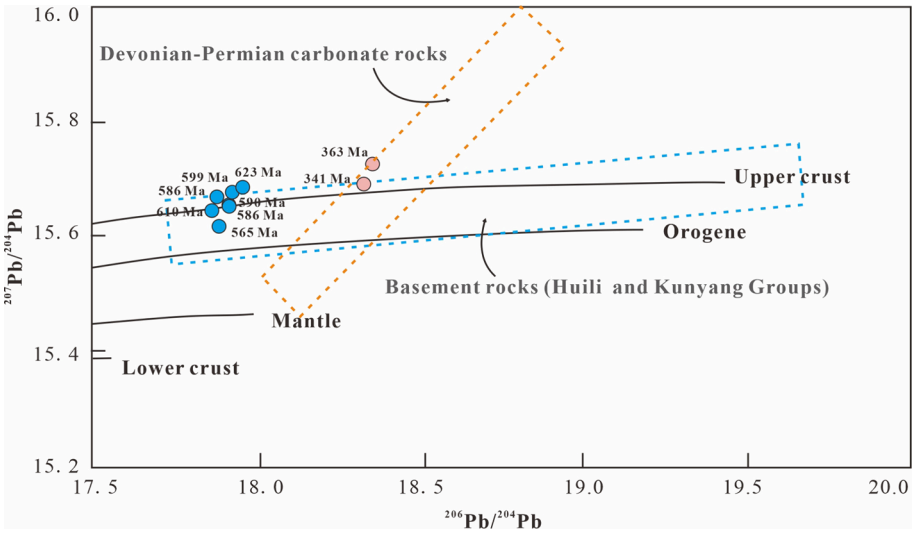

Fig. 8. Pb structure pattern of Pb-Zn ore in the DY Formation (Modified based on Zartman and Doe, 1981; Pb isotope ranges of Devonian-Permian carbonate rocks and basement rocks are quoted from Jin et al., 2016, Jin et al., 2017 Sulfide mineral samples with Pb-Pb ages ranging from 341 to 363 Ma fall within the Devonian-Permian carbonate rocks range and also fall above the growth line of the upper crust, representing the Pb source primarily originated from the upper crust; Sulfide mineral samples with Pb-Pb ages ranging from 565 to 623 Ma fall within the basement rocks range, and also fall below the growth line of the upper crust, representing the mixing Pb source of the mantle and the upper crust.

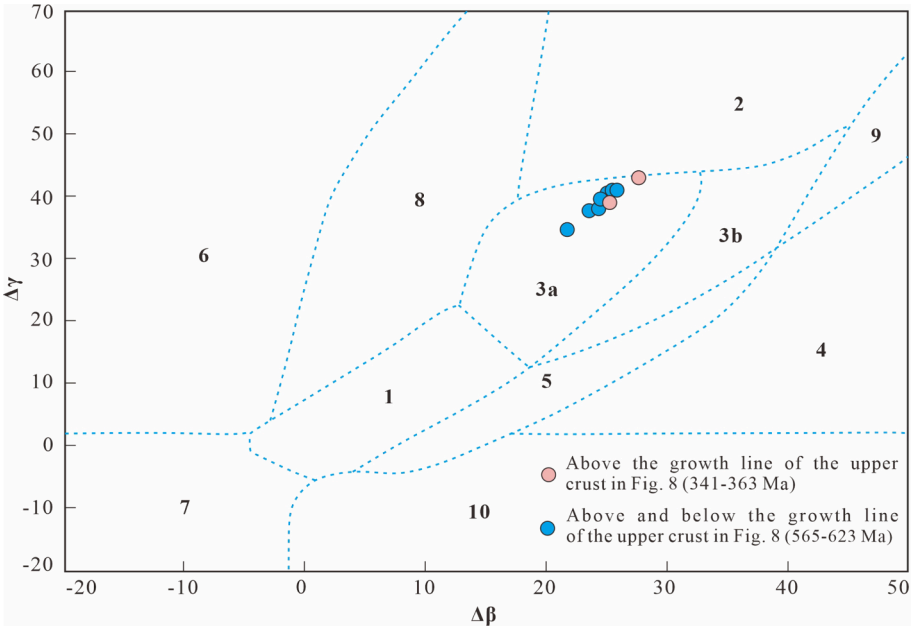

Fig. 9. Δβ-Δγ cross plot of Pb-Zn ore in the DY Formation (modified from Zhu, 1993, 1998) 1-mantle Pb; 2-upper crust Pb; 3-mixing Pb of upper crust and mantle in a subduction zone (3a-magmatism; 3b-sedimentation); 4-chemical deposition Pb; 5-hydrothermal Pb in seafloor; 6-middle-deep metamorphism Pb; 7-lower crust Pb in deep metamorphism; 8-orogenic Pb; 9-upper crust Pb in ancient shale; 10-retrogressive metamorphism Pb; All samples are located in the mixing Pb of the upper crust and mantle in subduction zone area, and are close to the upper crust Pb source area, representing the mixing Pb source of the upper crust and mantle. The samples with Pb-Pb ages ranging from 361 to 363 Ma are closer to the upper crust area, representing more contribution from upper crust Pb.

Formation temperature at 259.4 Ma was only about 120–145 °C (Gao et al., 2018; Yang et al., 2018), significantly lower than the temperature limit of crude oil cracking (>160 °C). However, the hydrothermal temperature in the DY Formation was higher than 200 °C (Fig. 5) and even reached 300 °C in certain areas (Zhang, 2019), providing a thermal condition for crude oil cracking. The CH_4-dominated gas inclusions trapped in Qz-2 and Sp-2 suggest oil cracking. Consequently, the solid bitumen in the DY Formation and the CH_4 trapped in Qz-2 and Sp-2 (formed after solid bitumen) were from the crude oil cracking under hydrothermal heating. The optical anisotropy of the solid bitumen corresponds with that of hydrothermally altered solid bitumen previously reported (Stasiuk, 1997).

Pressure change in the reservoir is another evidence of crude oil cracking. The Flincor software calculated fluid inclusion isochores by inputting homogeneous temperatures and salinities. The calculated isochores were used to estimate the minimum trapping pressure of fluid inclusions to evaluate the reservoir pressure at various hydrothermal stages. The results showed that the reservoir pressure was about 82 MPa at Stage I, while the pressure elevated abruptly to 183 MPa during Stage II (during the formation time of solid bitumen) (Fig. 7), comparable to the reservoir pressure calculated using methane inclusions by Fan et al. (2022). The significant increase in pressure was caused by a large amount of natural gas generated from rapid oil cracking. The substantial change in pressure and the filling sequences between solid bitumen, Dol-1, Sp-2, and galena can demonstrate that hydrothermal activity prompted the rapid oil cracking.

Table 3
Calculation results of Pb isotope parameters.

Sample	Sulfide mineral	μ	ω	κ	△β	△γ
GS7-1	pyrite	9.64	37.72	3.79	24.17	38.10
MX32-1		9.66	37.64	3.77	25.07	39.26
GS108-1	sphalerite	9.58	37.15	3.75	21.68	34.75
GS101-1		9.63	37.68	3.79	23.61	37.69
GS101-2		9.67	38.10	3.81	24.87	40.14
GS108-2		9.65	37.97	3.81	24.39	39.63
MX9-1		9.67	38.16	3.82	25.23	40.72
GS1-1		9.68	38.17	3.82	25.60	40.87
GS101-2	galena	9.73	38.27	3.81	27.54	43.16

5.2. *Ore-forming material sources*

5.2.1. *Metal source*

The Zartman-Doe structural pattern plate has been the most commonly used method for tracing the ore-forming metal source since the 1980 s (Zartman and Doe, 1981). Zartman and Doe found that the earth possesses three Pb reservoirs: the upper crust, the lower crust, and the upper mantle. The Pb reservoirs in the orogenic belt were formed through the component mixing of the crust and the mantle promoted by frequent orogenic activities. The ore-forming material source can be identified by placing the Pb isotope values on a Pb structural pattern plate (Stacey and Hedlund, 1983; Puig, 1988; Stendal, 1998). Some sulfide mineral samples lie above the growth line of the upper crust, indicating that the Pb primarily originated from the upper crust (Fig. 8). These samples also lie within the Devonian-Permian carbonate range, suggesting that they may originate from the Carboniferous and Devonian strata (Fig. 8). The remaining samples fall above and below the upper crustal growth line, showing the mixing origins of the upper crust and mantle (Fig. 8). These samples also lie within the range of basement rocks (Fig. 8), suggesting that the metal elements may originate from the underlying strata of the DY Formation.

Additionally, the variations in the thorium and Pb concentrations and the associations between the isotope compositions of thorium, Pb, and uranium can provide information for investigating geological processes and material sources. Zhu (1993, 1998) determined the Δβ-Δγ value ranges of various genetic Pb sources based on the analysis of different rocks and ores with known origins. This Δβ-Δγ chart reveals three Pb isotopes of ore and rock Pb as a relative deviation of the mantle simultaneously. The Δβ-Δγ chart shows that the Pb isotope values primarily fall in the mixing Pb of the upper crust and the mantle in the subduction zone, whereas the samples above the growth line of the upper crust in Fig. 8 are closer to the upper crust Pb area (Fig. 9). Consequently, samples (pink point) situated above the growth line of the upper crust have more upper crust Pb and other samples (blue point)

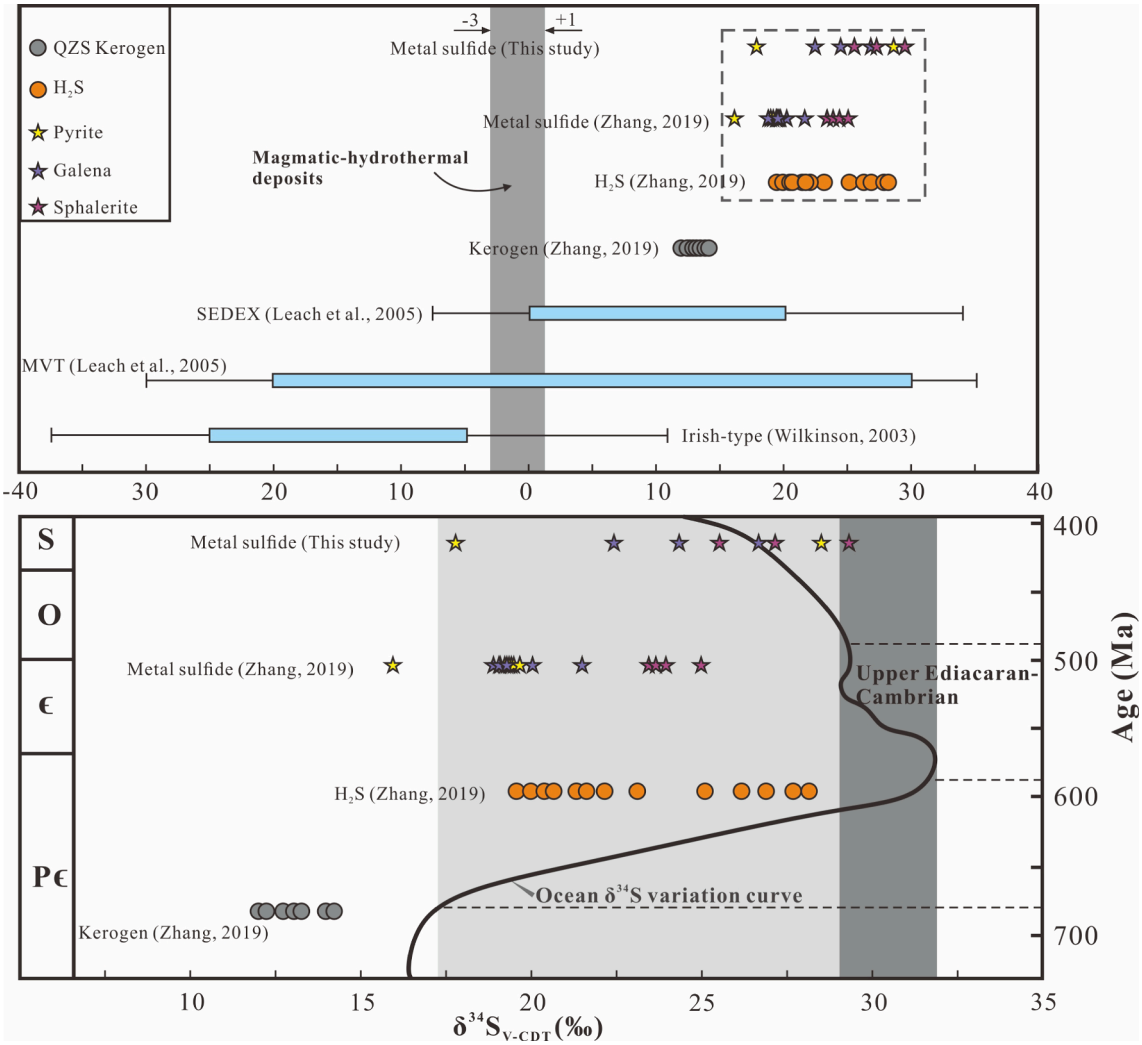

Fig. 10. Sulfur isotope compositions of sulfide minerals in the DY Formation *The sulfur isotope compositions of metal sulfide minerals are consistent with the sulfur isotope compositions of H_2S in DY Formation reservoirs and Precambrian seawater sulfate.*

have more mantle Pb, which is in line with the results of the Zartman-Doe Plate analysis. Therefore, the Pb-Zn deposits of the DY Formation have two ore-forming material sources: (1) predominantly the upper crust source; (2) the upper crust and mantle mixing source.

Pb-Pb age verified the metal sources. Normal Pb is Pb with a stable isotope composition in the same ore body, deposit, or mineralization area (isotope variation < 1.0 %) (Chen, 1978). The Pb isotope compositions of the sulfide minerals in the DY Formation are stable, with a slight variation range (<1.0 %), similar to the normal Pb. Geokit software (Lu, 2004) calculated Pb isotope parameters (Table 3). The results show that the μ ($^{238}U/^{204}Pb$) values range from 9.58 to 9.73 (mean value of 9.66), the ω ($^{232}Th/^{204}Pb$) values range from 37.15 to 38.27 (mean value of 37.87), and the κ ($^{232}Th/^{238}U$) values range from 3.75 to 3.82 (mean value of 3.80), which are typical isotope values of normal Pb (Tang et al., 2012; Du et al., 2022) (Table 3). Therefore, the ore Pb in the DY Formation is normal Pb, and the Pb-Pb age can be calculated using the single-stage evolution formula (Zhang et al., 2006; Zhang et al., 2009). The Holmes-Houtormans method is typically used to calculate the Pb-Pb age, which is more precise than other common Pb methods (Zhang et al., 2006; Zhang and Zhang, 2009). The estimated results show that the Pb ages of samples with the upper crust Pb range from 341 to 363 Ma, whereas the Pb ages of samples with the upper crust and mantle mixing Pb range from 565 to 623 Ma. These two age ranges are consistent with the age ranges of the strata where they are located in Fig. 8 (the Devonian-Permian and Pre-Ediacaran), confirming the dependability of the Pb source. Pb-Pb age still helps analyze the metal ore-forming mineral sources in the study area.

The first Pb source is the upper crust Pb, which has a similar Pb isotope composition as the Devonian-Permian carbonate. Caledonian tectonic movement can create conditions for this Pb source. Affected by the Caledonian tectonic movement, large-scale uplift occurred in central Sichuan, and the overlying strata of the Cambrian Formation were generally eroded (Xu et al., 2014; Li et al., 2014; Zou et al., 2014; Luo et al., 2015). The thickness of the residual strata overlying the DY Formation was only 50–70 m before the deposition of the Permian strata; thus, the surface karst fluids can enter the DY Formation (Mo et al., 2013; Peng, 2015). Studies have shown that those karst fluids led to a significant negative shift in the carbon and oxygen isotopes of the dolomites filling the pores and the host rocks (Zhang, 2013; Peng, 2014; Liang, 2014). Some scholars have also discovered karst deposits, blue-gray argillaceous dolomite, psammitic dolomite, and gravel-bearing dolomites from the weathering crust and upper Cambrian, and soft tongue snails, sponge bone needles, and colloidal phosphorus ore sands from the Lower Cambrian, in the DY reservoirs (Hou et al., 1999). These pieces of evidence are sufficient to demonstrate the karst fluid input during the Caledonian tectonic movement. The karst fluid on the surface eroded the strata to obtain metal elements before infiltrating into the DY reservoir along the fractures. The

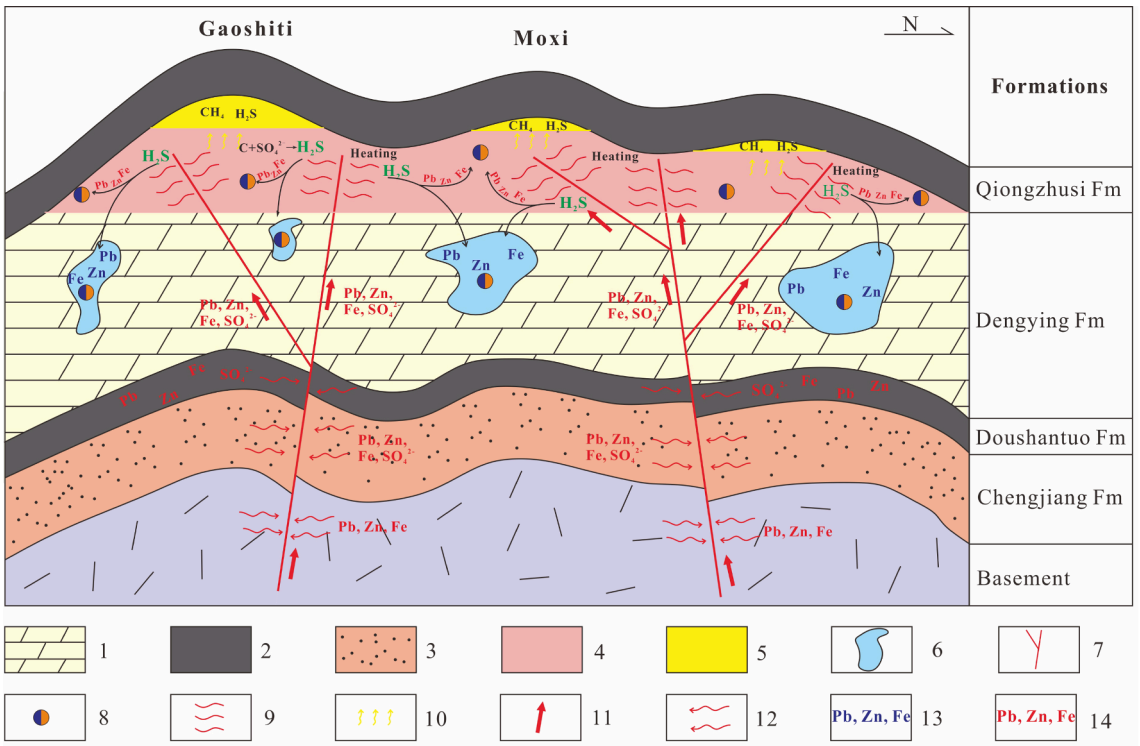

Fig. 11. Conceptual diagram of ore formation.

metal-rich karst fluid then mixed with the sealed seawater (early formation fluid) and remained in the DY reservoir (Xu, 2016). These metal elements in the mixing fluid are primarily derived from the overlying eroded carbonate and clastic rock of the DY Formation due to the very low Pb and Zn concentration in the sealed seawater (Yu, 2003; Wang et al., 2016). Therefore, some samples fall above the growth line of the upper crust, showing an upper crust origin.

The second Pb source is the upper crust and mantle mixing Pb, which has a similar Pb isotope composition as the Pre-Ediacaran strata. Hydrothermal fluids may be the only possible source of this Pb source. Hydrothermal fluids related to the Emeishan mantle plume continuously extracted metal elements from the sedimentary strata during upward migration, resulting in the mixing Pb source of the upper crust and mantle.

5.2.2. *Sulfur source*

All $\delta^{34}S$ values of sulfide minerals are positive, ranging from 16.1 ‰ to 29.3 ‰ (mean value of 22.64 ‰) (Table 1), significantly differing from those of magmatic-hydrothermal deposits (−3‰ to + 1 ‰) (Hoefs, 2009) while similar to these of SEDEX and MVT Pb-Zn deposits. The hydrothermal activity occurred in the late Permian (Su et al., 2020), whereas the DY Formation was buried nearly 2000 m deep at that time. Therefore, mineralization was later than diagenesis in the formation, suggesting that the Pb-Zn deposits in the DY Formation are not the SEDEX deposit but the MVT deposit consistent with a previous study (Zhang, 2019).

H_2S in the gas reservoir has two sources, organic and inorganic. The $\delta^{34}S$ values of inorganic H_2S are considerably lower than those of the H_2S remaining in the DY reservoir, at less than 5.5 %. Organic H_2S has three sources: biological sulfate reduction (BSR), kerogen or crude oil cracking, and TSR. The Raman analysis results of fluid inclusions demonstrate that H_2S in the reservoir formed during hydrothermal activity (Fig. 6). The reservoir temperature was approximately 129–152 ℃ when the hydrothermal activity occurred (259.4 Ma), surpassing the temperature at which BSR typically occurs (0–80 ℃). The $\delta^{34}S$ values of H_2S in the reservoir range from 16.1 ‰ to 29.3 ‰, which differ from those of the kerogen from the Qiongzhusi Formation, eliminating the kerogen cracking origin of those H_2S (Fig. 10). Therefore, H_2S in the reservoir is of TSR origin, consistent with previous studies (Zhu et al., 2015; Zhang et al., 2019). Sulfide minerals have similar $\delta^{34}S$ values as H_2S in the reservoir, indicating that the H_2S causing sulfide mineral precipitation is homologous to the H_2S in the reservoir (Fig. 10). The H_2S in the reservoir is residual after the Pb-Zn ore precipitation. Before hydrothermal input, liquid hydrocarbon had filled the reservoir (Fig. 4a), and the reservoir temperature increased to 129–152 ℃, which was suitable for TSR. Nevertheless, H_2S was detected in the fluid inclusions trapped in Qz-2 and Qz-L rather than Dol-F, indicating that the sulfate causing TSR was absent from the reservoir before hydrothermal activity. CO_2, the conventional TSR product, is also trapped together with H_2S in the inclusions (Orr, 1974; Machel, 2001). Therefore, the sulfate was more likely derived from the hydrothermal fluid. The coexistence of anhydrite and Dol-1 during the Pb-Zn mineralization indicates that the hydrothermal fluid has a high f_{O2} (Jiang et al., 2016; Gao, 2016). The Mn concentrations in sphalerite are subjected to redox conditions, with high Mn concentrations indicating a reduced environment while low Mn concentrations implying an oxidizing environment (Bernardini et al., 2004, Kelley et al., 2004; Zhuang et al., 2019). Mn concentration in DY sphalerite is less than 0.2 ppm (not published), suggesting a high f_{O2} of the hydrothermal fluids. Therefore, hydrothermal fluids can transport sulfate. Furthermore, the sulfur isotope compositions of H_2S and sulfide minerals correlate with those of Pre-Cambrian seawater, suggesting that sulfate was from the underlying strata of the ore deposits rather than from the mantle-derived fluid. Sulfate was extracted from the surrounding rock during the hydrothermal fluid migration. Large-scale strata deposited in evaporated tidal flat and lagoon facies are developed in the D-1 Member and the Doushantuo (DST) Formation

underlying the ore deposits (Ma et al., 2009; Wang, 2019). These formations were deposited under the evaporated environment, producing anhydrite and rock salt and sealing evaporated high-salinity seawater enriching sulfate. Hydrothermal fluids can interact with evaporated sulfate-rich high-salinity seawater while migrating through these strata, resulting in high salinity and high sulfate concentration in the hydrothermal fluid. Hydrothermal fluids passed through multiple sets of sulfate-enriched formations (such as Dol-1 and DST) during upward migration, and the sulfate in the hydrothermal fluids was a mixture of sealed evaporated high-salinity seawater within various formations. Therefore, hydrothermal sulfate has similar sulfur isotope compositions to the seawater from D-1 and DST (17 ‰–32 ‰) (Fig. 10), showing a broad isotope distribution range. Similar to the seawater from D-1 and DST, the H_2S remaining in the gas reservoir, pyrite, sphalerite, and galena also have a wide distribution range of sulfur isotopes.

5.3. Mineralization of mixing hydrothermal and hydrocarbon-bearing fluids

During the Caledonian tectonic movement, the strata in central Sichuan were commonly uplifted, and the overlying strata of the DY Formation were eroded (Mo et al., 2013; Peng, 2015). The surface karst fluid eroded the strata to obtain metal elements, infiltrated into the DY reservoir along the fractures, and mixed with the sealed seawater in the formation. Ore-forming metal from karst fluid was not altered due to the very low Pb and Zn concentration in the sealed seawater (Yu, 2003; Wang et al., 2016). Ore-forming metal was preserved in the DY reservoir without ore-forming conditions. During the middle-late Permian, the Qiongzhusi source rocks entered the oil generation window. A large amount of crude oil was produced and entered the DY reservoir to form paleo-oil reservoirs above the formation fluid at the top of D-2 and D-4. In the late Permian, large-scale hydrothermal activity occurred in the Sichuan Basin under the influence of the Emeishan mantle plume (Boven et al., 2002; Zhang et al., 2013; Yuan et al., 2014; Chen et al., 2012; Feng et al., 2017). Deep hydrothermal fluids migrated upward and extracted metal elements and sulfate from the wall rocks. After the hydrothermal fluid entered the oil layers in the DY Formation, the crude oil rapidly cracked under hydrothermal heating. TSR occurred between the hydrocarbons and the sulfate carried by the hydrothermal fluid and produced a large amount of H_2S, preferentially leading to the precipitation of nearby hydrothermal metals. Subsequently, the excess H_2S migrated down to the formation fluid layers with hydrothermal fluid to react with the metals brought by earlier karst fluid (Fig. 11). The generated H_2S was preferentially involved in mineralization with adjacent hydrothermal metals in the oil-bearing layers. The excessive H_2S completely precipitated the metals carried by the hydrothermal fluid before the hydrothermal fluid mixed with the formation fluid. Thus, these two ore-forming metal sources never mixed before mineralization, leading to distinct differences in Pb isotope compositions of these two types of Pb-Zn ores. After the Pb, Zn, and other ore-forming materials in the DY reservoir were depleted, the Pb-Zn mineralization ceased, and the residual H_2S remained in the reservoir alongside the natural gas.

6. Conclusions

(1) Hydrothermal fluid initiated the Pb-Zn mineralization in the DY Formation in central Sichuan during the late Permian. The hydrothermal stage can be divided into three: Stage I is recognized by saddle dolomite and pyrite; Stage II is identified by quartz and sphalerite, the main Zn mineralization stage; anisotropic solid bitumen formed during this stage; Stage III is primarily characterized by galena, the principal Pb mineralization stage.

(2) The Pb-Zn deposits of the DY Formation have two metal sources: the upper crust source, originated from the surface karst fluids; the upper crust and mantle mixing source, related to the hydrothermal fluids. The sulfur source was from TSR of the sulfate transported by hydrothermal fluids.

(3) The surface karst fluid eroded the strata to acquire metal elements and infiltrated into the DY reservoir to combine with the early formation fluid during the Caledonian tectonic movement. The metal ore-forming constituents were preserved in the DY reservoir. In the late Permian, a large amount of crude oil was produced by the Qiongzhusi Formation and entered the DY reservoir to form oil reservoirs over the formation fluid. Later, hydrothermal fluid related to the Emeishan mantle plume entered the reservoir. After the hydrothermal fluid entered the oil-rich layers, the crude oil rapidly cracked under hydrothermal heating. TSR occurred between the hydrocarbons in the reservoirs and the sulfate from the hydrothermal fluids, forming a large amount of H_2S that precipitated the metals from the hydrothermal and karst fluids. After the ore-forming materials (such as Fe, Pb, and Zn) were depleted, the residual H_2S was preserved with the natural gas in the reservoirs.

(4) This study has reconstructed the mineralization process caused by mixing between hydrothermal and hydrocarbon-bearing fluids. It utilized the study methods applied to petroleum geology to determine the hydrocarbon role in mineralization, providing a new perspective for the in-depth investigation of the Pb-Zn precipitation mechanism and the mineralization process related to hydrocarbon-bearing fluids.

CRediT authorship contribution statement

Lianqiang Zhu: Investigation, Writing – original draft. **Zezhang Song:** Data curation, Funding acquisition, Supervision. **Guangdi Liu:** Funding acquisition, Project administration, Supervision. **Wenzhi Zhao:** Validation, Supervision. **Long Wen:** Methodology. **Xingwang Tian:** Formal analysis. **Wenzhi Wang:** Conceptualization. **Dailin Yang:** Investigation. **Qiang Li:** Investigation.

Declaration of Competing Interest

The authors declare that they have no known competing financial interests or personal relationships that could have appeared to influence the work reported in this paper.

Data availability

Data will be made available on request.

Acknowledgements

This research was financially supported by the National Natural Science Foundation of China (Grant NO. 42272161, hydrothermal activities in deeply-buried and ultra-deeply-buried strata and the quantitative characterization of its alteration effect to paleo-oil reservoir) and Science Foundation of China University of Petroleum, Beijing (No. 2462023BJRC023). We would also thank the PetroChina Southwest Oilfield Company for providing core samples and necessary data.

References

Anderson, G.M., 2008. The mixing hypothesis and origin of Mississippi Valley-Type ore deposits. Econ. Geol. 103 (8), 1683–1690.
Anderson, G., 2015a. Kerogen as a source of sulfur in MVT deposits. Econ. Geol. 110, 837–840.
Anderson, G.M., 2015b. Kerogen as a source of sulfur in MVT deposits. Econ. Geol. 110 (3), 837–840.
Bernardini, G.P., Borgheresi, M., Cipriani, C., Di Benedetto, F., Romanelli, M., 2004. Mn distribution in sphalerite: an EPR study. Phys. Chem. Miner. 31 (2), 80–84.
Bodnar, R.J., 1990. Petroleum migration in the Miocene Monterey Formation, California, USA: Constraints from fluid inclusion studies. Mineral. Mag. 54 (375), 295–304.

Bodnar, R.J., 2003. Introduction to aqueous-electrolyte fluid inclusions. Fluid Inclusions: Analysis and Interprertation. 32, 81–100.
Boven, A., Pasteels, P., Punzalan, L.E., Liu, J., Luo, X., Zhang, W., Guo, Z., Hertogen, J., 2002. 40Ar/39Ar geochronological constraints on the age and evolution of the Permo-Triassic Emeishan Volcanic Province, Southwest China. J. Asian Earth Sci. 20, 157–175.
Burruss, R.C., 1981. Hydrocarbon fluid inclusions in studies of sedimentary diagenesis// Hollister, L.S., Crawford M L. Fluid inclusions: Applications to petrology. Mineralogical Association of Canada Short Course Handbook. 6, 138–156.
Chen, H.S., 1978. Theory and method of ore age determination by lead isotopes. Geol. Explor. 07, 9–20 in Chinese.
Chen, S.J., 1986. Discussion on the genesis of Pb-Zn deposits in western Guizhou and northeastern Yunnan. Geology of Guizhou. 3 (3), 211–222 in Chinese.
Chen, X., Zhao, W.Z., Zhang, L.P., Zhao, Z.J., Liu, Y.H., 2012. Discovery and exploration significance of structure–controlled hydrothermal dolomites in the Middle Permian of the central Sichuan Basin. Acta Pet. Sin. 33 (04), 562–569.
Cheng, K.M., Wang, S.Q., Dong, D.Z., Huang, J.L., Li, X.J., 2009. Accumulation conditions of shale gas in the Lower Cambrian Qiongzhusi Formation in the Upper Yangtze Region. Nat. Gas Ind. 29 (5), 40–44 in Chinese.
Chi, G., Kontak, D.J., Williams, A.E., 2004. Fluid composition and thermal regime during Zn–Pb mineralization in the Lower Nova Scotia. Canada. Geology. 93, 883–895.
Du, J.H., Zhang, B.M., Wang, Z.C., Zou, C.N., Xu, C.C., Shen, P., Zhang, J., Zhang, J., Zhou, H., Jiang, H., Wen, L., Shan, X.Q., Liu, J.J., 2016. The carbonate gentle slope of the Lower Cambrian Longwangmiao Formation in the Sichuan Basin Sedimentary model and reservoir genesis of grain beach. Nat. Gas Ind. 36, 1–10.
Du, B.F., Zhang, R.Z., Yang, C.Q., Li, S.P., Tan, H.Y., Zhu, H.Y., 2022. Sulfur and Lead Isotopic Compositions of the Zebuxia Pb–Zn Deposit in Tibet: Implications for the Sources of Ore–forming Material. Geoscience 1–10.
Eisenlohr, B.N., Tompkins, L.A., Cathles, L.M., Barley, M.E., Groves, D.I., 1994. Mississippi Valley–type deposits: products of brine expulsion by eustatically induced hydrocarbon generation? An example from northwestern Australia. Geology 22, 315–318.
Fan, J.J., Jiang, H., Lu, X.S., Liu, Q., Liu, S.B., Ma, X.Z., 2022. Pressure evolution and hydrocarbon accumulation process of Sinian Dengying Formation gas reservoirs in the Penglai area. SichuanBasin. Natural Gas Industry. 42 (12), 32–43.
Fazlia, S., Taghipoura, B., Moorea, F., Lentzb, D.R., 2019. Fluid inclusions, S isotopes, and Pb isotopes characteristics of the Kuh-eSurmeh carbonate-hosted Zn–Pb deposit in the Zagros Fold Belt, southwest Iran: Implications for the source of metals and sulfur and MVT genetic model. Ore Geol. Rev. 109, 615–629.
Feng, M.Y., Wu, P.C., Qiang, Z.T., Liu, X.H., Duan, Y., Xia, M.L., 2017. Hydrothermal dolomite reservoir in the Precambrian Dengying Formation of central Sichuan Basin. Southwestern China. Marine and Petroleum Geology. 82, 206–219.
Gao, P., 2016. Origin and Source of Sinian Bitumen in the Central Sichuan Basin. ChinaUniversity of Petroleum(Beijing). Doctor's thesis.
Gao, P., Liu, G.D., Wang, Z.C., Jia, C.Z., Wang, T.S., Zhang, R.W., 2017. Rare earth dements (REEs) geochemistry of Sinian-Cambrian reservoir solid bitumens in Sichuan Basin, SW China: potential application to petroleum exploration. Geol. J. 52, 298–316.
Gao, P., Liu, G.D., Lash, G.G., Li, B.Y., Yan, D.T., Chen, C., 2018. Occurrences and origin of reservoir solid bitumen in Sinian Dengying Formation dolomites of the Sichuan Basin, SW China. Int. J. Coal Geol. 200, 135–152.
Giordano, T.H., 2002. Transport of Pb and Zn by carboxylate complexes in basinal ore fluids and related petroleum–field brines at 100 ℃: the influence of pH and oxygen fugacity. Geochem. Trans. 3, 56–72.
He, B., Xu, Y.G., Xiao, L., Wang, K.M., Sha, S.L., 2003. The formation mechanism and spatial distribution of the Emeishan large igneous province: new evidence from sedimentary stratigraphy. Acta Geol. Sin. 02, 194–202.
Hoefs, J., 2009. Stable Isotope Geochemistry, sixth ed. Springer Verlag, Berlin, Heidelberg, pp. 130–135.
Hou, F.H., Fang, S.X., Wang, X.Z., Huang, J.X., Li, L., 1999. Further Understanding of the Natural Gas Reservoir Permeability Bodies in the Dengying Formation of the Sinian System in Sichuan Province. Acta Petrol. Sin. 20 (6), 16–21.
Hurtig, N.C., Hanley, J.J., Gysi, A.P., 2018. The role of hydrocarbons in ore formation at the Pillara Mississippi Valley-Type Zn–Pb deposit, Canning Basin. Western Australia. Ore Geology Reviews. 102, 875–893.
Jia, C.Z., 2007. The characteristics of intra-continental deformation and hydrocarbon distribution controlled by the Himalayan tectonic movements in China. Earth Sci. Front. 04, 96–104.
Jiang, Y.Q., Tao, Y.Z., Gu, Y.F., Wang, J.B., Qiang, Z.T., 2016. Hydrothermal dolomitization in Sinian Dengying Formation, Gaoshiti-Moxi area, Sichuan Basin. SW China. Petroleum Exploration and Development. 43 (01), 51–60.
Jin, Z.G., Zhou, J.X., Huang, Z.L., Luo, K., Gao, J.G., Peng, S., Wang, B., Chen, X.L., 2016. Ore genesis of the Nayongzhi Pb–Zn deposit, Puding City, Guizhou Province, China: Evidences from S and in situ Pb isotopes. Acta Petrol. Sin. 32 (11), 3441–3455.
Jin, Z.G., Zhou, J.X., Zheng, M.H., Peng, S., Huang, Z.L., Liu, L., 2017. Metallogenic model of Pb–Zn deposits in Wuzhishan area, Puding City. Guizhou Province. Mineral Deposits. 36 (5), 1169–1184.
Kelley, K.D., Leach, D.L., Johnson, C.A., Clark, J.L., Fayek, M., Slack, J.F., Anderson, V. M., Ayuso, R.A., Ridley, W.I., 2004. Textural, compositional, and sulfur isotope variations of sulfide minerals in the Red Dog Zn–Pb–Ag deposits, Brooks Range, Alaska: implications for ore formation. Econ. Geol. 99, 1509–1532.
Kesler, S.E., Jones, H.D., Furman, F.C., Sassen, R., Anderson, W.H., Kyle, J.R., 1994. Role of crude–oil in the genesis of Mississippi Valley-Type deposits—Evidence from the Cincinnati Arch. Geology 22, 609–612.
Kiyosu, Y., 1980. Chemical reduction and sulfur–isotope effects of sulfate by organic matter under hydrothermal conditions. Chem. Geol. 30 (1–2), 47–56.
Leach, D.L., Bradley, D.C., 2010. Sediment–hosted lead–zinc deposits in Earth history[J]. Econ. Geol. 105 (3), 593–625.
Leach, D.L., Sangster, D.F., Kelley, K.D., 2005. Sediment–hosted lead–zinc deposits: A global perspective. Econ. Geol. 100 (3), 561–607.
Lecumberri-Sanchez, P., Bouabdellah, M., Zemri, O., 2018. Transport of rare earth elements by hydrocarbon-bearing brines: Implications for ore deposition and the use of REEs as fluid source tracers. Chem. Geol. 479, 204–215.
Li, W., Y, H.Y., Hu, W.S., Yang, G., Xiong, X., 2014. Tectonic evolution of Caledonian paleohigh in the Sichuan Basin and its relationship with hydrocarbon accumulation. Natural Gas Industry. 34(03), 8–15.
Li, R.X., Mao, J.W., Zhao, B.S., 2021. A review of the role of hydrocarbon fluid in the ore formation of the MVT Pb–Zn deposit. Adv. Earth Science 36 (4), 335–345.
Li, Z.Q., Wang, X.Z., Ni, S.J., Li, C.Y., Hu, X.Q., Li, T.Y., 2002. Evidence of fluid Na–Cl–Br system from study on the source of ore-forming fluids in Mississippi Valley-type Pb-Zn deposits in Sichuan-Yunnan. Minerals and Rocks. 22 (4), 39–42 in Chinese.
Liang, J.J., 2014. The difference of hydrocarbon accumulation of Sinian and Lower Palaeozoic in the middle and southwest of Sichuan Basin. Chengdu University of Technology. Doctor's thesis.
Liu, S.G., Sun, W., Li, Z.W., Deng, B., Liu, S., 2008. Tectonic Uplifting and Gas Pool Formation since Late Cretaceous Epoch. Sichuan Basin. Natural Gas Geoscience. 03, 293–300.
Lu, Y.F., 2004. GeoKit: a package of geochemical tools built with VBA. Geochemistry 05, 459–464 in Chinese.
Luo, B., Luo, W.J., Wang, W.Z., 2015. The formation mechanism of Sinian gas reservoirs in Leshan-Longnüsi paleo–uplift. Sichuan Basin. Natural Gas Geoscience. 26 (03), 444–455.
Luo, K., Zhou, J.X., Ju, Y.W., 2022. A shift from BSR to TSR caused the formation of the Chipu Pb–Zn deposit. South China. Ore Geology Reviews. 144, 104845.
Ma, Y.S., Chen, H.D., Wang, L.G., 2009. Sequence stratigraphy and paleogeography in southern China. Science Press, Beijing.
Machel, H.G., 2001. Bacterial and thermochemical sulfate reduction in diagenetic settings—old and new insights. Sed. Geol. 140 (1–2), 143–175.
MacQueen, R.W., Powell, T.G., 1983. Organic geochemistry of the Pine Point lead–zinc ore field and region, Northwest-Territories. Canada. Economic Geology. 78, 1–25.
Mo, J., Wang, X.Z., Leng, S.Y., Lin, G., Xiong, J.W., 2013. Reservoir characteristics and control Factors of Sinian Dengying Formation in central Sichuan. Geol. China 40 (05), 1505–1514.
Ohmoto, H., 1972. Systematics of sulfur and carbon isotopes in hydrothermal ore deposits. Econ. Geol. 67 (5), 551–578.
Ohmoto, H., 1986. Stable isotope geochemistry of ore deposits. Rev. Mineral. Geochem. 16 (1), 491–559.
Ohmoto, H., Rye, R.O., 1979. Isotopes of sulfur and carbon. In: Barnes, H.L. (Ed.), Geochemistry of Hydrothermal Ore Deposits. Wiley, New York, pp. 509–567.
Orr, W.L., 1974. Changes in sulfur content and isotopic ratios of sulfur during petroleum maturation study of Big Horn Basin Paleozoic oils. AAPG Bull. 58, 2295–2318.
Ostendorf, J., Henjes-Kunst, F., Mondillo, N., Boni, M., Schneider, J., Gutzmer, J., 2015. Formation of Mississippi Valley–type deposits linked to hydrocarbon generation in extensional tectonic settings: evidence from the Jabali Zn-Pb-(Ag) deposit (Yemen). Geology 43, 1055–1058.
Pelch, M.A., Appold, M.S., Emsbo, P., Bodnar, R.J., 2015. Constraints from fluid inclusion compositions on the origin of Mississippi Valley–type mineralization in the Illinois– Kentucky district. Economical Geology. 110, 787–808.
Peng, B., 2014. The development mechanism and controlling factors of Dengying Formation reservoir in the Central -Southern Sichuan basin. Chengdu University of Technology. Doctor's thesis.
Peng, B., 2015. The development mechanism and controlling factors of Dengying Formation reservoir in the Central-Southern Sichuan basin. Chengdu University of Technology. Doctoral thesis.
Puig, A., 1988. Geologic and metallogenic significance of the isotopic composition of lead in galenas of the Chilean Andes. Econ. Geol. 83, 843–858.
Saintilan, N.J., Spangenberg, J.E., Samankassou, E., Kouzmanov, K., Chiaradia, M., Stephens, M.B., Fontbote, L., 2016. A refined genetic model for the Laisvall and Vassbo Mississippi Valley–type sandstone–hosted deposits, Sweden: constraints from paragenetic studies, organic geochemistry, and S, C, N, and Sr isotope data. Miner. Deposita 51, 639–664.
Selby, D., Creaser, R.A., Dewing, K., Fowler, M., 2005. Evaluation of bitumen as a ^{187}Re–^{187}Os geochronometer for hydrocarbon maturation and migration: a test case from the Polaris MVT deposit. Canada. Earth Planetary Science Letters. 235, 1–15.
Sicree, A.A., Barnes, H.L., 1996. Upper Mississippi Valley district ore fluid model: the role of organic complexes. Ore Geology Reviewer. 11, 105–131.
Sośnicka, M., Lüders, V., 2019. Super–deep, TSR–controlled Phanerozoic MVT type Zn–Pb deposits hosted by Zechstein–2 gas reservoir carbonate (Ca_2), Lower Saxony Basin Germany. Chem. Geol. 508, 62–77.
Stacey, J.S., Hedlund, D.C., 1983. Lead–isotope compositions of diverse igneous rocks and ore deposits from southwestern New Mexico and their implications for early Proterozoic crustal evolution in the western United States. Geol. Soc. Am. Bull. 94, 43–57.
Stasiuk, L.D., 1997. The origin of pyrobitumens in upper Devonian Leduc formation gas reservoirs, Alberta, Canada: an optical and EDS study of oil to gas transformation. Mar. Pet. Geol. 14, 915–929.
Stendal, H., 1998. Contrasting Pb isotopes of Archaean and Palaeoproterozoic sulphide mineralization, Disko Bugt, central West Greenland. Miner. Deposita 33, 255–265.
Su, A., Chen, H.H., Feng, Y.X., Zhao, J.X., Nguyen, A.D., Wang, Z.C., Long, X.P., 2020. Dating and zcharacterizing primary gas accumulation in Precambrian dolomite reservoirs, Central Sichuan Basin, China: Insights from pyrobitumen Re–Os and dolomite U-Pb geochronology. Precambr. Res. 350, 105897.

Tang, S.K., Ma, X., Li, X.G., Dai, C.G., Zhang, H., Zhou, Q., Kuang, S.D., Yang, K.G., 2012. Study on Pb isotopes of the Fulaichang Pb-Zn deposit in northwestern Guizhou and its geological significance. Geotecton. Metallog. 36 (4), 549–558 in Chinese.
Wang, G.Z., Liu, S.G., Chen, C.H., 2013. The genetic relationship between MVT Pb–Zn deposits and paleo–oil/gas reservoirs at Heba. Southeastern Sichuan Basin. Earth Science Frontiers. 20 (1), 107–116.
Wang, Z.C., Liu, J.J., Jiang, H., Huang, S.P., Wang, K., 2019. Lithofacies paleogeography and exploration significance of Sinian Doushantuo depositional stage in the middle-upper Yangtze region, Sichuan Basin. SW China. Petroleum Exploration and Development. 46 (01), 39–51.
Wang, X.N., Wang, Z.H., Chen, Y.N., 2016. Determination of Pb, cadmium and copper in seawater by solid phase extractioncoupled with graphite furnace atomic absorption spectroscopy. Chin. J. Anal. Lab. 35 (01), 1157–1160.
Wei, G.Q., Xie, Z.Y., Song, J.R., Yang, W., Wang, Z.H., Li, J., Wang, D.L., Li, Z.S., Xie, W. R., 2015. Sinian-Cambrian natural gas characteristics and genesis of the central Sichuan paleo-uplift in the Sichuan Basin. Pet. Explor. Dev. 42, 702–711.
Wu, Y., Zhang, C.Q., Mao, J.W., Zhang, W.S., Wei, C., 2013. The Relationship between Oil–gas Organic Matter and MVT Mineralization: A Case Study of the Chipu Lead–zinc Deposit. Sichuan. Acta Geoscientica Sinica. 34 (4), 425–436.
Xu, F.H., 2016. Fluid system and hydrocarbon accumulation of Sinian Dengying Formation and Cambrian Longwangmiao Formation in central Sichuan. Chengdu University of Technology. Doctor's thesis.
Xu, C.C., Shen, P., Yang, Y.M., Luo, B., Huang, J.Z., Jiang, X.F., Xie, J.R., Cen, Y.J., 2014. The natural gas accumulation conditions and enrichment rules of the Sinian-Lower Cambrian Longwangmiao Formation in the Leshan-Longnüsi paleo–uplift. Nat. Gas Ind. 34, 1–7.
Yang, C.Y., Ni, Z.Y., Li, M.J., 2018. Pyrobitumen in South China: Organic petrology, chemical composition and geological significance. Int. J. Coal Geol. 188, 56–63.
Yang, C.Y., Li, M.J., Wang, T.G., Zhong, N.N., Fang, R.H., 2023. Texture development of mesophase in reservoir pyrobitumen and the temperature-pressure converting of the gas reservoir in the Chuanzhong Uplift. Southwestern China. Petroleum Science. 20 (2), 721–732.
Yang, Y.M., Wen, L., Luo, B., 2016a. Hydrocarbon accumulation of Sinian natural gas reservoirs, Leshan-Longnvsi paleohigh, Sichuan Basin SW China. Pet. Explor. Dev. 43 (2), 179–188.
Yang, Y.M., Wen, L., Luo, B., Wang, W.Z., Shan, S.J., 2016b. Hydrocarbon accumulation of Sinian natural gas reservoirs, Leshan-longnusi paleohigh, Sichuan Basin SW China. Pet. Explor. Dev. 43 (02), 179–188.
Yu, T., 2003. Study about dissolved heavy metals and their background values in South China Sea. 3, 329-333.
Yuan, B., Mao, J.W., Yan, X.H., Wu, Y., Zhang, F., Zhao, L.L., 2014a. Sources of metallogenic materials and metallogenic mechanism of Daliangzi Ore Field in Sichuan Province: Constraints from geochemistry of S, C, H, O, Sr isotope and trace element in sphalerite. Acta Petrol. Sin. 30 (1), 209–220.
Yuan, B., Mao, J.W., Yan, X.H., Wu, Y., Zhang, F., Zhao, L.L., 2014b. The source and mechanism of zmineralization of the Daliangzi lead–zinc deposit: Sulfur, carbon, hydrogen, oxygen, strontium isotopes and the restriction of sphalerite trace elements. Acta Petrol. Sin. 30, 209–220.
Zartman, R.E., Doe, B.R., 1981. Plumbotectonics–the model. Tectonophysics 75, 135–162.
Zhang, S., 2013. Study on the Formation Mechanism of the High-quality Reservoir of Dengying Formation in Middle of Sichuan Basin Gaoshiti Structure. Chengdu University of Technology. Master's thesis.
Zhang, C.Q., Li, H.M., Dai, J.Z., Yang, X.C., Li, L., Mao, J.W., Yu, J.J., Lou, D.B., 2006. Lead isotope research on lead–zinc deposits. Mineral Deposits 25 (S1), 213–216 in Chinese.
Zhang, C.Q., Li, X.H., Yu, J.J., Mao, J.W., Chen, F.K., Li, H.M., 2008. Rubidium–strontium dating of sheet-grain sphalerite from Daliangzi Pb-Zn deposit, Sichuan and its geological significance. Geological Review. 54 (4), 145–151 in Chinese.
Zhang, P.W., Liu, G.D., Cai, C.F., Li, M.J., Chen, R.Q., Gao, P., Xu, C.L., Wan, W.C., Zhang, Y.Y., Jiang, M.Y., 2019. Alteration of solid bitumen by hydrothermal heating and thermochemical sulfate reduction in the Ediacaran and Cambrian dolomite reservoirs in the Central Sichuan Basin. SW China. Precambrian Research. 321, 277–302.
Zhang, C.Q., Rui, Z.Y., Chen, Y.C., Wang, D.H., Chen, Z.H., Lou, D.B., 2013. Pb–zinc mineral resource potential and main strategic continuation areas in China. Chinese Geology. 40, 248–272.
Zhang, J.H., Zhang, G.Y., 2009. A review of the application of lead isotopes in ore deposit research and prospecting. Geological Prospecting Issues. 24 (4), 322–328 in Chinese.
Zhang, P.Y., 2019. Study on the genesis mechanism of hydrogen sulfide in Sinian Cambrian gas reservoir in Central Sichuan region. University of petroleum of China (Beijing). Doctoral thesis.
Zhao, D., Han, R.S., Wang, L., Ren, T., Wang, J.S., Zhang, X.P., Cui, J.H., Ding, J.J., 2021. Genesis of the Lehong large zinc–lead deposit in northeastern Yunnan, China: Evidences from geological characteristics and C-H–O–S–Pb isotopic compositions. Ore Geol. Rev. 135, 104219.
Zhou, J.G., Zhang, J.Y., Deng, H.Y., Chen, Y.N., Hao, Y., Li, W.Z., Gu, M.F., Luo, X.Y., 2017. Lithofacies paleogeography and sedimentary model of the Sinian Dengying Formation in Sichuan Basin. Nat. Gas Ind. 37, 24–31.
Zhu, B.Q., 1993. Three-dimensional spatial topology diagram of Pb isotopes in ore for geochemical province and mineral division. Geochemistry 3, 209–216 in Chinese.
Zhu, B.Q., 1998. Theory and Application of Isotope System in Earth Science—Also on the Evolution of China Continental Crust and Mantle. Science Press (in Chinese), Beijing.
Zhu, L.Q., Liu, G.D., Song, Z.Z., Zhao, W.Z., Li, Q., Tian, X.W., Wang, Y.L., Yang, D.L., 2022. Reservoir solid bitumen–source rock correlation using the trace and rare earth elements–implications for identifying the natural gas source of the Ediacaran-Lower Cambrian reservoirs, central Sichuan Basin. Mar. Pet. Geol. 137, 105499.
Zhu, G.Y., Wang, T.S., Xie, Z.Y., Xie, B.H., Liu, K.Y., 2015. Giant gas discovery in the Precambrian deeply buried reservoirs in the Sichuan Basin, China: implications for gas exploration in old cratonic basins. Precambr. Res. 262, 45–66.
Zhuang, L.L., Song, Y.C., Liu, Y.C., Fard, M., Hou, Z.Q., 2019. Major and trace elements and sulfur isotopes in two stages of sphalerite from the world–class Angouran Zn–Pb deposit, Iran: implications for mineralization conditions and type. Ore Geol. Rev. 109, 184–200.
Zou, C.N., Du, J.H., Xu, C.C., Wang, Z.C., Zhang, B.M., 2014. Formation, distribution, resource potential and discovery of the Sinian– Cambrian giant gas field, Sichuan Basin. SW China. Petroleum Exploration and Development. 41 (3), 278–293.